

# The large-scale cross-correlation of Damped Lyman Alpha Systems with the Lyman Alpha Forest: First Measurements from BOSS

**Andreu Font-Ribera<sup>a,b</sup> , Jordi Miralda-Escudé<sup>c,d</sup> , Eduard Arnau<sup>d</sup> , Bill Carithers<sup>b</sup> , Khee-Gan Lee<sup>e</sup> , Pasquier Noterdaeme<sup>f</sup> , Isabelle Pâris<sup>f,g</sup> , Patrick Petitjean<sup>f</sup> , James Rich<sup>h</sup> , Emmanuel Rollinde<sup>f</sup> , Nicholas P. Ross<sup>b</sup> , Donald P. Schneider<sup>i,j</sup> , Martin White<sup>b,k</sup> and Donald G. York<sup>l</sup>**

<sup>a</sup>Institute of Theoretical Physics, University of Zurich, 8057 Zurich, Switzerland

<sup>b</sup>Lawrence Berkeley National Laboratory, University of California, Berkeley, California 94720, USA

<sup>c</sup>Institució Catalana de Recerca i Estudis Avançats, Catalonia

<sup>d</sup>Institut de Ciències del Cosmos (IEEC/UB), Barcelona, Catalonia

<sup>e</sup>Max-Planck-Institut für Astronomie, Königstuhl 17, D-69117 Heidelberg, Germany

<sup>f</sup>Université Paris 6 et CNRS, Institut d'Astrophysique de Paris, 98bis blvd. Arago, 75014 Paris, France

<sup>g</sup>Departamento de Astronomía, Universidad de Chile, Casilla 36-D, Santiago, Chile

<sup>h</sup>CEA, Centre de Saclay, IRFU, 91191 Gif-sur-Yvette, France

<sup>i</sup>Department of Astronomy and Astrophysics, The Pennsylvania State University, University Park, PA 16802

<sup>j</sup>Institute for Gravitation and the Cosmos, The Pennsylvania State University, University Park, PA 16802

<sup>k</sup>Departments of Physics and Astronomy, 601 Campbell Hall, University of California Berkeley, CA 94720, USA

<sup>l</sup>Department of Astronomy and Astrophysics and The Fermi Institute, University of Chicago, 5640 So. Ellis Ave., Chicago, IL 60637, USA

E-mail: [font@physik.uzh.ch](mailto:font@physik.uzh.ch)

**Abstract.** We present the first measurement of the large-scale cross-correlation of Ly $\alpha$  forest absorption and Damped Lyman  $\alpha$  systems (DLA), using the 9th Data Release of the Baryon Oscillation Spectroscopic Survey (BOSS). The cross-correlation is clearly detected on scales up to  $40 h^{-1}$  Mpc and is well fitted by the linear theory prediction of the standard Cold Dark Matter model of structure formation with the expected redshift distortions, confirming its origin in the gravitational evolution of structure. The amplitude of the DLA-Ly $\alpha$  cross-correlation depends on only one free parameter, the bias factor of the DLA systems, once the Ly $\alpha$  forest bias factors are known from independent Ly $\alpha$  forest correlation measurements. We measure the DLA bias factor to be  $b_D = (2.17 \pm 0.20)\beta_F^{0.22}$ , where the Ly $\alpha$  forest redshift distortion parameter  $\beta_F$  is expected to be above unity. This bias factor implies a typical host halo mass for DLAs that is much larger than expected in present DLA models, and is reproduced if the DLA cross section scales with halo mass as  $M_h^\alpha$ , with  $\alpha = 1.1 \pm 0.1$  for  $\beta_F = 1$ . Matching the observed DLA bias factor and rate of incidence requires that atomic gas remains extended in massive halos over larger areas than predicted in present simulations of galaxy formation, with typical DLA proper sizes larger than 20 kpc in host halos of masses  $\sim 10^{12} M_\odot$ . We infer that typical galaxies at  $z \simeq 2$  to 3 are surrounded by systems of atomic clouds that are much more extended than the luminous parts of galaxies and contain  $\sim 10\%$  of the baryons in the host halo.

**Keywords:** cosmology: large-scale structure — cosmology: intergalactic medium — cosmology: galaxy formation — quasars: absorption systems

---

## Contents

<b>1</b>	<b>Introduction</b>	<b>1</b>
<b>2</b>	<b>Data</b>	<b>3</b>
2.1	The DLA catalogue	3
2.2	$\text{Ly}\alpha$ forest spectra	6
<b>3</b>	<b>Method</b>	<b>7</b>
3.1	Continuum fitting	7
3.2	Mean transmitted fraction	8
3.3	Mean transmission correction	9
3.4	Estimator and covariance matrix of the cross-correlation	11
3.5	Sub-samples and bootstrap errors	13
3.6	Fitting the DLA bias	15
<b>4</b>	<b>Results</b>	<b>16</b>
4.1	Measured cross-correlation and bias parameter	17
4.2	Effect of the MTC	17
4.3	Tests of the covariance matrix	20
4.4	Evidence for the redshift distortions	21
4.5	Scale dependence of the DLA bias	22
4.6	Effect of the DLAs on the $\text{Ly}\alpha$ forest	23
4.7	Dependence on the $\text{Ly}\alpha$ bias	23
4.8	Redshift evolution	24
4.9	Dependence on column density	25
4.10	Result for the sample affected by BAL Contamination	25
<b>5</b>	<b>Discussion</b>	<b>25</b>
5.1	Constraints on the halo mass distribution from the bias factor	26
5.2	Constraints on the cross sections from the rate of incidence	28
5.3	Consequences for the nature of DLAs	28

<b>6</b>	<b>Conclusions</b>	<b>30</b>
<b>A</b>	<b>Effect of the Mean Transmission Correction on the cross-correlation</b>	<b>34</b>
<b>B</b>	<b>Optimal quadratic estimator</b>	<b>37</b>
B.1	Definitions and notation	37
B.2	General solution	39
B.3	Approximations	39

---

## 1 Introduction

Damped Ly $\alpha$  systems, defined as absorption systems with neutral hydrogen column density  $N_{HI} \geq 2 \times 10^{20} \text{ cm}^{-2}$  (hereafter referred to as DLAs), are a powerful probe of the physical evolution of gas that has condensed to high density to become self-shielded and atomic, and is presumably in the process of forming galaxies. Spectroscopic surveys of quasars to search for DLAs are usually performed at  $z > 2$ , because the absorption spectra can be observed from the ground at wavelengths longer than the atmospheric cutoff. These surveys have revealed the rate of incidence of DLAs to be  $\sim 0.2$  per unit of redshift at  $z = 3$ , slowly increasing with redshift, and their total gas content to be close to  $\Omega_{DLA} \simeq 10^{-3}$ , or a few percent of all the baryons in the universe (see the review [1]). This baryonic mass of DLAs is about one third of all the mass that is contained today in stars [2, 3], and is comparable to the mass of stars that had formed in the universe by  $z = 2$  (although the total stellar mass at this redshift is substantially uncertain; see [4], for a review).

These observational facts suggest that DLAs are connected with the gas clouds that are responsible for forming galaxies at high redshift. Moreover, they imply that once the gas that has gravitationally collapsed into dark matter halos becomes self-shielded against ionizing radiation and mostly atomic, it must either remain in atomic form in the DLAs for a time comparable to the Hubble time before forming stars, or else be ionized, expelled, and continuously replaced by other gas accreting onto halos and recombining. The reason is that if atomic gas were to quickly form molecular clouds and stars soon after recombining, then its baryonic content would always be much smaller than that of stars during the entire epoch of galaxy formation. At the same time, the total cross section for intersecting DLAs is much larger than the fraction of the sky covered by the starlight-emitting regions of observed galaxies. Therefore, large reservoirs of atomic gas must remain orbiting in halos for long periods of time, either covering wide areas around the galaxies where star formation is most active, or remaining stable in numerous low-mass halos with little star formation.

Despite these powerful observational constraints, the precise nature of DLAs remains poorly known, primarily because the mass of their host halos and the type of galaxies they are associated with has not been observationally determined. The observed rate of incidence tells us the product of the number density of DLA systems times their cross section, but these two quantities are not separately known. In reality, there can be a diverse population of objects with a wide range of cross sections giving rise to the observed DLAs. In the context of the Cold Dark Matter model of structure formation by hierarchical merging of

halos, we can define a mean proper cross section  $\Sigma(M, z)$  of a halo of mass  $M$  at redshift  $z$  for producing a DLA in the spectrum of a background source. The observed rate of incidence of DLA absorbers per unit redshift,  $R(z)$ , is given by

$$R(z) dz = \frac{c(1+z)^2}{H(z)} \int_0^\infty dM n(M, z) \Sigma(M, z) dz, \quad (1.1)$$

where  $n(M, z) dM$  is the comoving number density of halos of mass  $M$  within the mass range  $dM$ , and  $H(z)$  is the Hubble constant at redshift  $z$ . The observational determination of any diagnostic of the halo mass associated with specific DLAs has generally proved extremely difficult. One of the possible avenues is to detect the galaxy associated with a DLA absorber. Recent progress in the selection strategies and observational techniques has allowed for several detections (see [5] and references therein), but the sample size remains very limited owing to the faintness of the associated galaxies and the additional difficulty involved in detecting them at a very small impact parameter from a bright quasar.

Another method of characterizing the population of halos that are hosting the DLA absorbers is through the large-scale clustering amplitude. In the limit of large scales, any population of objects that traces the primordial mass perturbations has a correlation function that is proportional to the mass autocorrelation in the linear regime,  $\xi_m(r)$ . Hence, the autocorrelation of DLA absorbers on large scales in real space is  $\xi_D(r) = b_D^2 \xi_m(r)$ , where  $b_D$  is the *bias factor* of DLA absorbers. The bias factor of halos of mass  $M$ ,  $b_h(M, z)$ , can be computed by means of approximate analytic models (e.g., [6]) and accurately predicted with numerical simulations [7]. The bias factor of the DLA absorbers is related to that of halos by

$$b_D(z) = \frac{\int_0^\infty dM n(M, z) \Sigma(M, z) b_h(M, z)}{\int_0^\infty dM n(M, z) \Sigma(M, z)}. \quad (1.2)$$

In general, the bias factor of halos increases with their mass: halos collapsing out of rare, high peaks, with a mass much higher than that of a typical halo, are highly clustered [8]. Any measurement of the correlation amplitude of DLAs can be a powerful probe of the characteristic halo mass hosting the DLAs: the higher the value of the bias, the more massive their typical host halos need to be.

Measuring the bias factor of DLA absorbers requires either measuring their autocorrelation, or their cross-correlation with another tracer population. The principal obstacle for measuring the clustering amplitude of DLAs has been the sparseness of quasars at  $z > 2$  that are bright enough to allow for spectroscopy to detect DLAs in absorption; in addition, only  $\sim 10\%$  of observed quasars yield a detected DLA. The first measurement of the clustering of DLAs was performed in [9] using the cross-correlation with luminous Lyman break galaxies, by measuring redshifts of Lyman break galaxies identified in deep imaging of fields around 9 quasars with 11 known DLAs in their absorption spectra. Their result was that the bias factor of DLAs is in the range  $1.3 < b_D < 4$ . The large uncertainty is due to the small size of their DLA sample, which is difficult to increase because of the large observing time required to map the area around each DLA.

The Baryon Oscillations Spectroscopic Survey (BOSS,[10]) in the SDSS-III Collaboration [11] provides a new opportunity for an accurate measurement of the clustering of DLAs. With a tenfold increase of the number of known quasars at  $z > 2$  compared to previous

surveys, and a similar increase in the number of detected DLAs, we can attempt to cross-correlate the DLAs with any other objects that are measured in the available quasar spectra over the same redshift range: these are the DLAs themselves, quasars, the Ly $\alpha$  forest, and metal line absorbers. Because of the low density of quasars, we can measure these correlations more easily on large scales, corresponding to the typical separation between neighboring BOSS quasars on the sky of 15', or about  $15\ h^{-1}\text{Mpc}$  (comoving), instead of the smaller scales that are probed by deep imaging of Lyman break galaxies in the area adjacent to targeted DLAs. Measurements on large scales have the advantage that accurate predictions for the correlations can be obtained from linear theory. These large-scale correlations can also be measured for metal-line absorbers, and a first detection has already been presented by [12].

In this paper, we measure the cross-correlation of DLAs with the Ly $\alpha$  forest transmitted flux fraction. This turns out to be the cross-correlation that yields the most accurate measurement of the bias factor of DLAs, because of the large number of independent Ly $\alpha$  forest fluctuations that are probed on every line of sight to a quasar. This cross-correlation is proportional to the product of a bias factor for DLAs and a bias factor for the Ly $\alpha$  forest. The Ly $\alpha$  forest bias factor is independently derived from the observed autocorrelation of the Ly $\alpha$  forest transmitted flux [13], and therefore the DLA bias factor can be robustly inferred from our measurement. We describe the sample of DLAs and Ly $\alpha$  forest spectra used for our analysis in section 2. The detailed method for measuring the DLA-Ly $\alpha$  forest cross-correlation is presented in section 3, and the results for the cross-correlation and the inferred bias factor of the DLAs are presented in section 4. Finally the results are discussed in section 5.

Throughout this paper we use the flat  $\Lambda$ CDM cosmology, with  $\Omega_m = 0.281$ ,  $\Omega_b = 0.0462$ ,  $h = 0.71$ ,  $n_s = 0.963$  and  $\sigma_8 = 0.8$ , similar with the best-fit parameters obtained from the WMAP analysis in [14]. We note that the values of the bias factors we quote for the Ly $\alpha$  forest and for DLAs vary in inverse proportion to the assumed value of  $\sigma_8$ .

## 2 Data

This study uses the quasar catalogue of the Data Release 9 (DR9,[15]) of the Baryon Oscillation Spectroscopic Survey (BOSS, [10]), which is part of SDSS-III Collaboration ([11], [16], [17], [18], [19], [20]). The catalogue, described in detail in [21], contains a total of 61931 quasars at  $z > 2.15$ . The target selection procedure used for identifying the quasar candidates for BOSS spectroscopy was presented in [22], and uses the methods described in [23], [24], and [25].

We now describe the sample of DLAs found in the spectra of these quasars and the set of Ly $\alpha$  forest spectra that we use for measuring the DLA-Ly $\alpha$  cross-correlation.

### 2.1 The DLA catalogue

Our analysis is based on a subset of the DLA catalogue of [26]. Here we briefly summarize the DLA detection method and refer the reader to [27] for further details. DLAs are searched in each line of sight over a redshift range between  $z_{min}$ , defined as the redshift where the

spectral signal-to-noise ratio per pixel, averaged over a  $2000 \text{ km s}^{-1}$  window, reaches 2, and the quasar redshift. For the purpose of detecting DLAs, the quasar continuum is modeled by fitting a modified power-law with smoothly changing index plus Moffat profiles on top of the emission lines. The data is correlated with synthetic profiles of increasing column densities in order to detect DLA candidates and obtain a first guess of the  $N_{HI}$ . Whenever the system has associated metal lines, these are used to further improve the accuracy of the DLA redshift. Finally, the column density is obtained by fitting a Voigt-profile to the data.

The overall DLA catalogue contains a total of 12081 DLA candidates with  $\log N_{HI} \geq 20$ . For the purpose of measuring the DLA incidence rate and the total amount of neutral gas in the Universe, a statistical sample optimized to achieve high completeness was defined by [26], where systematic effects can be quantified using mock data. Here, a high purity of the catalogue is our greatest concern to measure the cross-correlation because any inclusion of objects that are not real DLAs may systematically decrease the measured amplitude of the cross-correlation. Completeness, on the other hand, is less important because eliminating a fraction of the real DLAs will increase the error of, but not systematically modify, the cross-correlation.

The first cut we apply is to eliminate DLAs outside the redshift range  $2.0 < z < 3.5$ . The few DLAs that are outside this redshift range have very few nearby lines of sight with good signal-to-noise ratio in which the cross-correlation can be measured, so we eliminate them in order to have a well defined redshift interval of our systems. The standard definition of a DLA is an absorption system with a column density  $N_{HI} \geq 10^{20.3} \text{ cm}^{-2}$  [28], so strictly speaking, the systems we use below this column density are sub-DLAs. We decide, however, to adopt a threshold of a factor of two below this definition because (i) systems down to  $10^{20} \text{ cm}^{-2}$  are robustly identified and are not expected to sharply change their nature with column density and (ii) our measurement of the cross-correlation increases in accuracy with the number of systems available. In this paper we refer to all of the systems used for our cross-correlation measurement, with  $N_{HI} > 10^{20} \text{ cm}^{-2}$ , as DLAs (however, when discussing rates of incidence and baryon contents of DLAs later in section 5, these quantities will refer to systems with  $N_{HI} > 10^{20.3} \text{ cm}^{-2}$ ). Systems of even lower column density are less reliably detected. We shall see in section 4 that we do not detect any dependence of the clustering properties with column density. The number of DLAs that satisfy these criteria is 10512.

The second cut requires that the continuum-to-noise ratio (CNR) of the quasar spectrum is larger than three. The continuum-to-noise ratio is defined as the median value of the ratio of the fitted continuum in the DLA detection analysis in [26] to the noise per pixel, over the observed Ly $\alpha$  forest region for each quasar spectrum. This provides a good estimate of the data quality over the region of interest, while being independent of the presence of an absorber. We find this criterion to be a good threshold for ensuring the purity of our sample without excessively reducing the number of systems. The number of DLAs that survive this second cut is 9288.

The rest of the cuts we apply involve eliminating Broad Absorption Line systems (hereafter, BALs) that produce broad spectral troughs which, at the low signal-to-noise ratio of most of the BOSS spectra, are not easily distinguished from the Voigt profiles of DLAs with the superposed Ly $\alpha$  forest. Our third cut eliminates all DLAs found in quasars classified as BALs in the visual inspection of the DR9 quasars described in [21], leaving 8469 DLAs. In addition, in order to remove any BAL contaminants near the Ly $\alpha$  emission line that may be

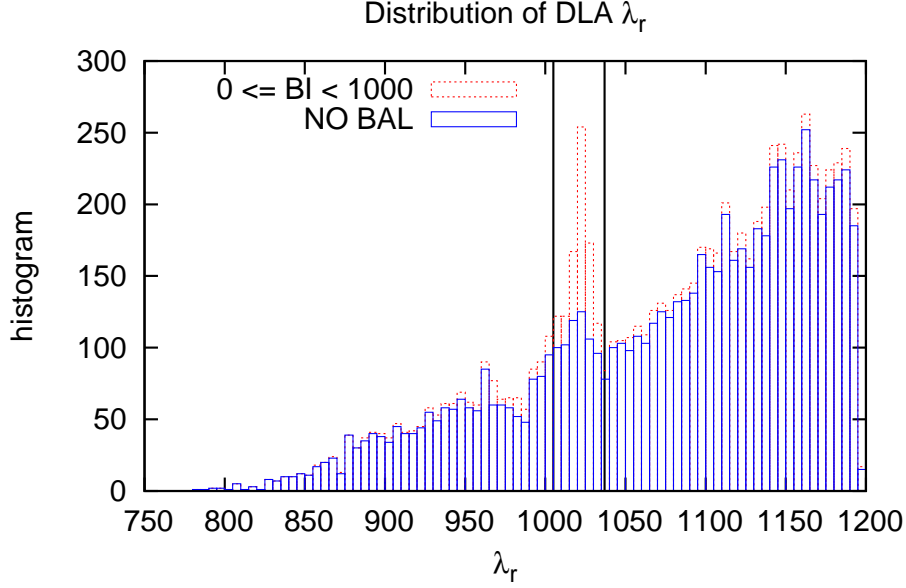


**Figure 1.** Quasar rest-frame wavelength distribution of the DLAs that satisfy the criteria of redshift and column density range, continuum to noise ratio and velocity separation from the background quasar. The red histogram (8189 systems) contains also quasars with BAL systems with a Balnicity index  $BI < 1000 \text{ km s}^{-1}$ , while the blue histogram (7458 systems) contains no systems flagged as BAL. Vertical lines show the cut applied to our final sample,  $1005 \text{ \AA} \leq \lambda_r \leq 1037 \text{ \AA}$ , reducing to 6780 the final number of DLAs used in this study.

too weak to have been identified, our fourth cut eliminates all the DLAs that are within a velocity separation  $v < 5000 \text{ km s}^{-1}$  from the quasar redshift, where

$$\frac{v}{c} = \frac{z_q - z_D}{1 + z_q} = \frac{\lambda_\alpha - \lambda_r}{\lambda_\alpha}, \quad (2.1)$$

$z_q$  and  $z_D$  are the redshifts of the quasar and the DLA,  $\lambda_\alpha$  is the  $\text{Ly}\alpha$  wavelength, and  $\lambda_r$  is the quasar rest-frame wavelength at which the DLA absorption line is centered. Equivalently, this condition is  $\lambda_r < 1196 \text{ \AA}$ . Application of this constraint reduces the number of DLAs to 7458. We emphasize that most of the 1011 systems eliminated in this velocity range are probably real DLAs, but we prefer to eliminate them because they probably contain a substantial fraction of BAL absorbers among them.

Figure 1 shows the distribution of  $\lambda_r$  for the 7458 DLAs passing all of the above cuts as the blue (solid) histogram. The red (dotted) histogram shows the same distribution when BALs with a Balnicity Index  $BI < 1000 \text{ km s}^{-1}$  ([29]) are included. The histograms clearly show an excess of DLAs in the interval indicated by vertical black lines in figure 1. Moreover, quasars with weak BALs are much more common in this interval than at other values of  $\lambda_r$ . This strongly suggests that this excess is due to BAL contamination from the  $\text{Ly}\beta$  and OVI absorption lines, and that additional BALs that may be stronger in OVI than in CIV and other detectable lines are probably lurking among the DLAs identified in this interval of  $\lambda_r$ . We therefore apply a fifth cut, eliminating all the DLAs in this interval, with a maximum wavelength  $\lambda_r < 1037 \text{ \AA}$  chosen equal to the longest wavelength member of the OVI doublet,



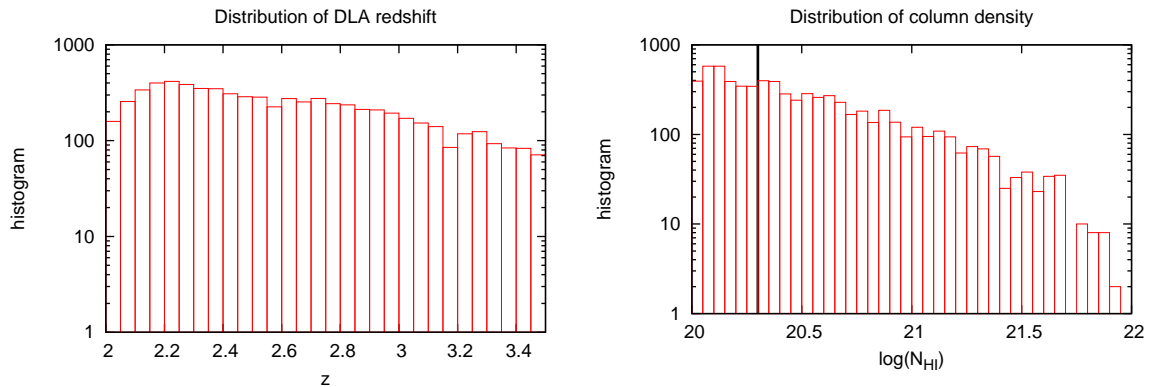


**Figure 2.** Left panel: distribution of the 6780 DLA redshifts. Right panel: neutral hydrogen column density distribution. The vertical line on the right panel corresponds to the standard lower limit for DLAs,  $\log N_{HI} > 20.3$ .

and a minimum wavelength  $\lambda_r > 1005 \text{ \AA}$ , corresponding to a velocity  $v < 6000 \text{ km s}^{-1}$  to the blue of the  $\text{Ly}\beta$  line. This restriction reduces our DLA sample to 6780 systems. In section 4, we shall show that the bias factor measured for the DLAs found in this interval is in fact much smaller than the ones outside, confirming a large degree of contamination by BAL systems.

The column density and redshift distributions of the final set of DLAs selected for our study are plotted in figure 2. The redshift distribution of the DLAs used for our measurement of the cross-correlation with the  $\text{Ly}\alpha$  forest peaks at  $z \simeq 2.2$  and declines smoothly as a function of redshift.

## 2.2 $\text{Ly}\alpha$ forest spectra

We select quasars in the redshift range  $2.15 < z < 3.5$  for the  $\text{Ly}\alpha$  forest spectra to be correlated with the DLA positions. The total number of DR9 quasars in this redshift range is 58722. We eliminate all the spectra that are identified as BAL, and we also make a signal-to-noise ratio cut requiring a median  $S/N > 0.5$  per pixel in the rest-frame wavelength interval  $1220 \text{ \AA} \leq \lambda_r \leq 1600 \text{ \AA}$ . The number of spectra that are left after these cuts is 52449.

The co-added spectra released in DR9 are used, removing any pixels that do not pass the bit mask and the sky mask as defined in [30]. For this study we define the  $\text{Ly}\alpha$  forest region as the pixels with a rest-frame wavelength in the range  $1041 \text{ \AA} \leq \lambda_r \leq 1185 \text{ \AA}$ .

A total of 3047 of these lines of sight contain at least one DLA in the  $\text{Ly}\alpha$  forest region. For most of our results we include these lines of sight for our estimate of the cross-correlation of DLAs with the  $\text{Ly}\alpha$  absorption, using the correction explained in [30] for removing the DLA from the  $\text{Ly}\alpha$  absorption, where the central region of the DLA is masked and the wings are corrected using a Voigt profile with the best estimate of the column density. As shown in section 4.6, rejecting these lines of sight does not significantly change the results. Since DLAs are not easily identified in low S/N spectra, we expect some residual contamination of DLAs in our  $\text{Ly}\alpha$  sample.

### 3 Method

This section describes first the determination of a continuum model for each quasar to infer the Ly $\alpha$  absorption field. The method we use to compute the cross-correlation of DLAs with the Ly $\alpha$  forest and its covariance matrix, and to fit a parameterized linear theory model to the result, is then presented. We use the co-added quasar spectra of DR9 selected as explained in section 2, which contain combined exposures from a single plate after applying interpolated sky subtraction and flux calibration corrections [10, 16]. The observed flux  $f_i$  at each pixel  $i$  at wavelength  $\lambda_i = \lambda_\alpha (1 + z_i)$  (where  $\lambda_\alpha$  is the Ly $\alpha$  wavelength and  $z_i$  is the Ly $\alpha$  absorption redshift) is the product of the quasar continuum  $C_i$  and the transmitted flux fraction  $F_i$ , plus the noise  $N_i$  that we approximate as Gaussian with variance  $\langle N_i^2 \rangle$ , as provided by the pipeline [16],

$$f_i = C_i F_i + N_i \equiv C_i \bar{F}(z_i) [1 + \delta_{Fi}] + N_i, \quad (3.1)$$

where  $\bar{F}(z_i)$  is the mean value of  $F$  as a function of redshift, and  $\delta_{Fi}$  is the Ly $\alpha$  transmission perturbation. Our analysis of the correlation will use the variable  $\delta_{Fi}$ , where often the pixel subindex  $i$  will be dropped for brevity.

#### 3.1 Continuum fitting

We use the Principal Component Analysis (PCA) technique described in [31] for fitting a continuum to each quasar. A set of PCA quasar templates with eight components is used to do a least-squares fit on each quasar spectrum in the  $1216 \text{ \AA} \leq \lambda_r \leq 1600 \text{ \AA}$  region to obtain an estimate for the continuum, using equation (3) of [31]. The total number of parameters used is 11 (eight for PCA eigenvalues, one for the flux normalization, and two for a redshift and mean spectral slope corrections; see Table 1 of [31]). The PCA templates that are used span the wavelength interval  $1020 \text{ \AA} \leq \lambda_r \leq 1600 \text{ \AA}$ , so a predicted continuum in the Lyman  $\alpha$  forest region can then be obtained by extrapolating the fit to  $\lambda_r < 1216 \text{ \AA}$ .

This procedure is repeated for two sets of quasar templates. The first was generated by [32] using HST ultraviolet spectra of 50 low-redshift quasars, where the Ly $\alpha$  forest continuum is easily estimated because of the low mean absorption. The second was generated by [33] from 78 SDSS DR7 ([34]) quasars with high signal-to-noise ratio, where the continua were fitted with a low-order spline function. The use of these different templates ensures full coverage of the luminosity range spanned by the BOSS quasars. The best of the two fits obtained from these two template sets is then selected, which we designate as  $C_i^{PCA}$ . For the DR9 quasars we use, the set of templates from [32] turns out to provide the best fit for  $\sim 85\%$  of the quasars.

An additional step was applied in [31], referred to as *mean flux regulation*, where each quasar continuum was multiplied by a second order polynomial with two parameters that were fitted to match the mean flux evolution from [35]. This mean flux regulation substantially reduces the variance of the Ly $\alpha$  absorption field, owing to the removal of spectrophotometric errors and of any quasar intrinsic spectral diversity that is not accounted for by the PCA templates. However, large-scale power in the Ly $\alpha$  forest is also suppressed by this process in a way that is complex and difficult to model. For this reason, we do not apply the mean flux regulation procedure here. Instead, a more simple *mean transmission correction* (MTC)

is applied that is described below in section 3.3, which affects the measured cross-correlation with DLAs in a way that is easier to correct for.

### 3.2 Mean transmitted fraction

For the purpose of measuring the cross-correlation of the Ly $\alpha$  forest with DLAs, it is important to ensure that the average value of the transmission perturbation  $\delta_F$  at each redshift is precisely zero. If this condition is not imposed, the value of the cross-correlation will differ from zero in the limit of large scales simply because an incorrect value of  $\bar{F}$  is being used.

For this reason, we measure the mean transmitted fraction in 50 redshift bins of  $\Delta z = 0.03$  linearly spaced in redshift between  $z = 1.9$  and  $z = 3.4$ , by computing the weighted average of the flux in all the pixels in each redshift bin  $k$ , centered at redshift  $z'_k$ ,

$$\bar{F}^{PCA}(z'_k) = \frac{\sum_{i \in k} w'_i f_i / C_i^{PCA}}{\sum_{i \in k} w'_i}, \quad (3.2)$$

where the sums are done over all the pixels  $i$  with a redshift  $z_i$  within the redshift bin  $k$ . The weights are equal to the total inverse variance of  $f_i / C_i^{PCA}$ ,

$$w'_i = \left[ \bar{F}_e(z_i)^2 \sigma_F^2(z_i) + \frac{\langle N_i \rangle^2}{(C_i^{PCA})^2} \right]^{-1}, \quad (3.3)$$

where  $\sigma_F^2 = \langle \delta_F^2 \rangle$  is the intrinsic variance of the Ly $\alpha$  forest, and  $\bar{F}_e(z)$  is an externally determined value of the mean transmitted fraction as a function of redshift, for which we use the result of [35]. Because these weights do not need to be obtained to very high accuracy, we do not iterate equations (3.2) and (3.3) to calculate the weights using the values of  $\bar{F}^{PCA}$  instead of  $\bar{F}_e$ . For the intrinsic variance as a function of redshift, we use the simple expression

$$\sigma_F^2(z) = 0.065 [(1+z)/3.25]^{3.8}, \quad (3.4)$$

based on the redshift evolution of the power spectrum measured in [36].

Figure 3 shows the mean transmitted fraction  $\bar{F}^{PCA}$  (red dashed line) compared to the result of [35] (blue dotted line). Our measurement is very close to that of [35], and is typically higher by only  $\sim 1\%$ . In addition, there are sharp features in the inferred  $\bar{F}(z)$ : the bump at  $z = 2.6$ , and several other rapid fluctuations at lower redshift. These features are a systematic error that arises from the calibration of the spectra using F stars which are particularly important in the Balmer stellar absorption lines. Each observed plate in BOSS has a set of calibration stars that are used to translate photon counts in the CCD to flux units [10]. The spectra of these stars are masked near the Balmer lines, and this introduces an artifact in the calibration vector. A similar artifact was present in earlier SDSS data ([37]), but the effect seems to be larger in BOSS, as noted by [38]. This systematic is being studied and will be corrected in the future.

The small difference between our measured  $\bar{F}(z)$  and that in [35] may also be caused by errors in the zero-flux level computed by interpolating from neighboring fibers used for sky subtraction ([21]), or to other calibration systematic effects ([16]), but these errors are not a problem for our study of the cross-correlation as long as they are not correlated in any way with the presence of DLAs on nearby lines of sight. The black solid line in Figure 3 is  $\bar{F}(z)$  in our redshift bins after the MTC is applied, which we describe next.

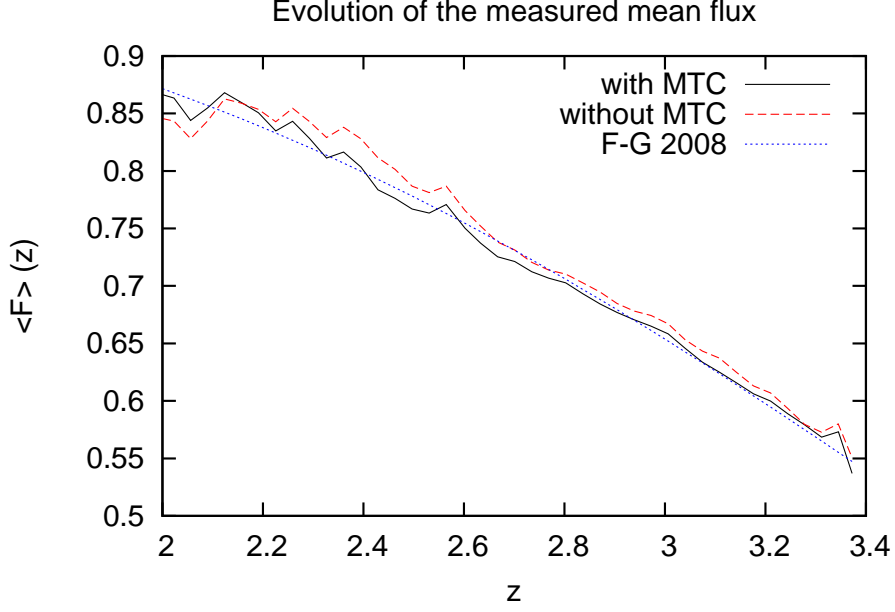


**Figure 3.** Measured mean transmission as a function of redshift, with (solid black line) and without (dashed red line) the Mean Transmission Correction, compared to the measurement of [35] (blue dotted line).

### 3.3 Mean transmission correction

The same errors that can produce a difference in the mean transmission  $\bar{F}^{PCA}$  and the value  $\bar{F}_e$  from [35] imply the presence of stochastic errors in any single quasar spectrum that can systematically bias our estimated value of  $\delta_F$  on large scales along the line of sight. This may substantially increase the noise in our cross-correlation measurement. As a test of this effect, we measure the variance of the weighted average of  $\delta_F$  over the whole Ly $\alpha$  spectrum of a single quasar, which we find to be on average equal to 0.03.

The expected variance from the Ly $\alpha$  forest alone depends on the quasar redshift, both because of the different comoving length of the forest and because of the evolution of the line of sight power with redshift. However, for  $z < 2.8$  the expected variance is always below 0.001. Even though metal lines and Lyman limit systems should increase this variance, they cannot account for a value as large as 0.03, which we infer mostly reflects the random variation from quasar to quasar of the systematic miscalibration. A variance of 0.03 on the mean of  $\delta_F$  over a spectrum can be induced by an rms variation of the continuum amplitude of  $\sim 17\%$ .

With the aim of eliminating this additional source of noise, we apply a *Mean Transmission Correction* (MTC) to the PCA continuum fit, which we compute for each quasar spectrum as

$$A_q = \frac{\sum_{i \in q} w'_i f_i / [C_i^{PCA} \bar{F}_e(z_i)]}{\sum_{i \in q} w'_i}, \quad (3.5)$$

where the sums are performed over all pixels  $i$  in the Ly $\alpha$  forest region (as defined in section

2) of a quasar  $q$ , and the weights are computed with equation (3.3). The corrected quasar continuum is

$$C_i \equiv C_i^{PCA} A_q , \quad (3.6)$$

and the corrected transmission fraction at each pixel is

$$F_i \equiv \frac{f_i}{C_i} = \frac{f_i}{C_i^{PCA} A_q} . \quad (3.7)$$

The corrected average mean transmission  $\bar{F}(z'_k)$ , computed as in equation (3.2) but with the corrected continua, is now even closer to  $\bar{F}_e(z)$ , as shown in Figure 3. The correction also reduces the variance of  $\delta_F$ , even at the pixel level. This effect is shown in Figure 4, where the variance before the MTC correction is shown as the dashed red line, and after the MTC correction as the black solid line. When the contribution to the variance from the noise provided by the BOSS pipeline, after we apply a wavelength-dependent correction as explained in [30], is subtracted from this MTC-corrected variance, the short-dash green line is obtained. This line should correspond to the intrinsic variance of the Ly $\alpha$  forest. The value of the variance we obtain in this way is still higher than the expected intrinsic variance from equation (3.4), shown as the dotted blue line, but the difference is small and is probably explained by residual errors in the continuum fit, metal lines and Lyman limit systems.

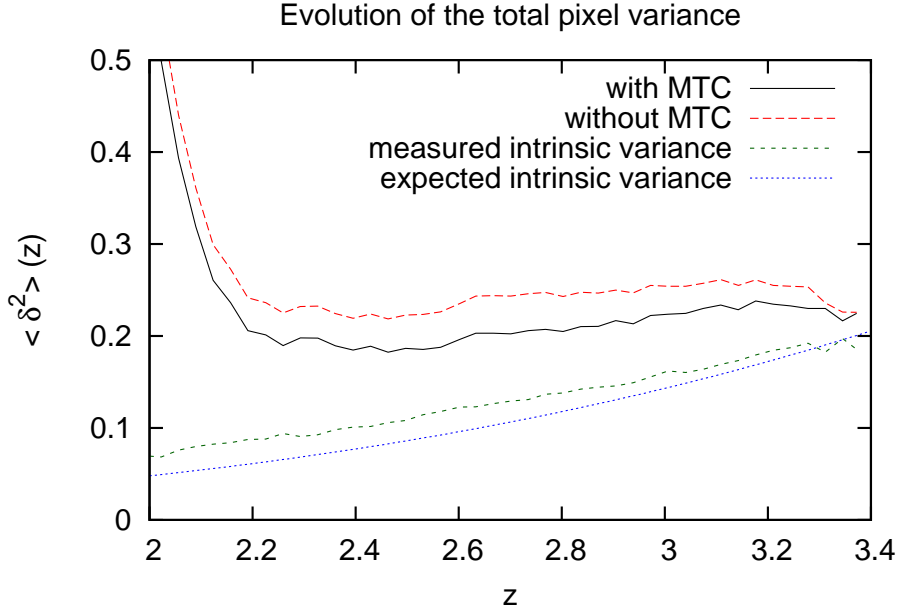


**Figure 4.** Measured variance per pixel with MTC (solid black line) and without (long-dashed red line). The inferred intrinsic variance using the MTC assuming the corrected noise variance provided by the pipeline is shown by the short-dashed green line, and the intrinsic variance assumed for the weights [eq. (3.4)] is the dotted blue line.

Our estimator for the fluctuation in the transmitted flux fraction,  $\delta_F$ , is obtained at every pixel as

$$\delta_{Fi} = \frac{f_i}{C_i \bar{F}(z_i)} - 1 , \quad (3.8)$$

where  $\bar{F}(z_i)$  is the mean transmission that has been obtained in the redshift bin which contains the pixel redshift  $z_i$ . By construction, the average of  $\delta_{Fi}$  at a given redshift bin is zero. Because  $\bar{F}(z_i)$  is close to  $\bar{F}_e(z_i)$ , the average of  $\delta_{Fi}$  over each individual quasar spectrum is also nearly zero. The MTC is therefore approximately the same operation as forcing the weighted average of  $\delta_F$  to be zero on each individual quasar spectrum by subtracting its mean value.

Subtracting the mean value of  $\delta_F$  in each line of sight removes some of the large-scale power of the Ly $\alpha$  transmission field. This subtraction was also applied in [13] for measuring the Ly $\alpha$  transmission autocorrelation, and an analytical expression to correct for its effect on the correlation function was presented in their Appendix A. We compute an equivalent expression of this correction to the measured cross-correlation of DLAs and the Ly $\alpha$  forest in our Appendix A.

Unless otherwise specified, our results will incorporate the MTC, and the DLA bias parameter will be fitted including the MTC correction of our theoretical models that is derived in Appendix A. However, results without including the MTC will also be presented and discussed.

### 3.4 Estimator and covariance matrix of the cross-correlation

The simplest method is used in this paper to obtain an estimator for the cross-correlation of DLAs and the Ly $\alpha$  forest,  $\hat{\xi}_A$ : we compute the weighted average of  $\delta_F$  over all the pixels located at a separation from a DLA that is within a bin  $A$  of  $\mathbf{r}_A$ ,

$$\hat{\xi}_A = \frac{\sum_{i \in A} w_i \delta_{Fi}}{\sum_{i \in A} w_i}. \quad (3.9)$$

The summation symbols in this equation indicate a double sum: first over all the DLAs, and then over all the pixels at a separation within the  $A$  bin from the DLA. Consequently, the value of  $w_i \delta_{Fi}$  of one pixel appears repeated several times in the sum whenever the pixel is within the separation bin  $A$  from several DLAs. The DLAs are all weighted equally, and the Ly $\alpha$  pixels are weighted as the inverse of their total variance, including the noise contribution and the intrinsic variance:

$$w_i = \left[ \sigma_F^2(z_i) + \frac{\langle N_i^2 \rangle}{C_i^2 \bar{F}_e^2(z_i)} \right]^{-1}. \quad (3.10)$$

The method is similar to the one used by [13] for measuring the Ly $\alpha$  forest transmission autocorrelation. There are a number of assumptions and simplifications involved in the use of the simple equation (3.9) for the estimator of the cross-correlation:

1. The correlations among the values of  $\delta_F$  in neighboring pixels (both along a single line of sight and along nearby, parallel lines of sight) can be neglected for the purpose of optimizing the weights. We take into account these correlations below for the purpose of computing the covariance matrix of the cross-correlation, but we neglect them for obtaining an optimal estimator by choosing the simple weights in equation (3.10).

2. We assume that the DLAs can be detected with a probability that is independent of their large-scale environment, and therefore independent of the mean Ly $\alpha$  forest absorption that is superposed on their damped wings.

Neither of these two assumptions is precisely correct. Failure of the first one makes our measurement suboptimal, but does not bias it in any way. The optimal manner to estimate the cross-correlation is discussed in Appendix B, where the assumptions involved in obtaining the simplified estimator in equation (3.9) are analyzed and discussed in more detail. The second assumption is required to avoid a systematic bias of this estimator: if DLAs are more likely to be detected when the forest absorption is higher, then the cross-correlation is artificially enhanced. We believe this second effect is small enough to be neglected, because tests have shown that the cross-correlation amplitude is not affected above the continuum-to-noise ratio that we impose on our sample (section 2.1). We nevertheless plan to make a correction for this effect in the future by testing how the probability of DLA detection with a specific algorithm is modified by the superposition of the Ly $\alpha$  forest on the damped wings, using mock Ly $\alpha$  spectra that include DLAs with a biased distribution relative to the Ly $\alpha$  forest [39].

The measurement of the cross-correlation with equation (3.9) is done using 16 bins in the radial separation  $\pi$ , and 8 bins in the transverse separation  $\sigma$ . To test for the symmetry of the cross-correlation under a sign change of  $\pi$ , we use different bins for negative and positive  $\pi$ , where  $\pi$  is positive when the pixel of the Ly $\alpha$  forest transmission perturbation is at higher redshift than the DLA. The bins in  $\pi$  are, in units of comoving  $h^{-1}$  Mpc, bounded by the values  $(-60, -40, -30, -20, -15, -10, -6, -3, 0)$  and the same positive values, while the bins in  $\sigma$  are bounded, in the same units, by  $(1, 4, 7, 10, 15, 20, 30, 40, 60)$ . Pairs at transverse separation  $\sigma < 1 h^{-1}$  Mpc are not used (the number of these pairs is negligibly small in our sample). This results in a total of 128 separation bins in  $\sigma$  and  $\pi$ . The weighted average values of  $(\pi, \sigma)$  of all the contributing pixel-DLA pairs to every bin are stored, with the same weights as in equation (3.10) (these are generally close but not exactly equal to the central values of each bin). The measurement is generally done using a single bin of the mean redshift  $z$  of the Ly $\alpha$  forest pixel and the DLA, which is required to be in the range  $2.0 < z < 3.5$ , although we also present some results in the next section using three redshift bins.

The covariance of the cross-correlation measured with equation (3.9) in two bins  $A$  and  $B$  is equal to

$$\tilde{C}_{AB} \equiv \langle \hat{\xi}_A \hat{\xi}_B \rangle - \langle \hat{\xi}_A \rangle \langle \hat{\xi}_B \rangle = \frac{\sum_{i \in A} \sum_{j \in B} w_i w_j C_{ij}}{\sum_{i \in A} w_i \sum_{j \in B} w_j}, \quad (3.11)$$

where  $C_{ij} = \langle \delta_{Fi} \delta_{Fj} \rangle$  is the correlation of the measured values of  $\delta_F$  in pixels  $i$  and  $j$ , separated in redshift space by  $\mathbf{r}_{ij}$ . Note that the correlation  $C_{ij}$ , with two subindexes for the two correlated pixels, should not be confused with the quasar continuum which always has one subindex, and the covariance matrix of the cross-correlation,  $\tilde{C}$ , is a different matrix with indexes referring to bins in  $(\pi, \sigma)$ . There are three main contributions to the correlation  $C_{ij}$ : the intrinsic autocorrelation of the Ly $\alpha$  forest at a given separation  $\xi_F(\mathbf{r}_{ij})$ , the noise term  $\langle N_i^2 \rangle / (C_i^2 \bar{F}_i^2)$  that we assume to be uncorrelated among different pixels, and continuum



fitting errors with a correlation  $\xi_c(r_{ij})$  that affect only pairs of pixels in the same spectrum,

$$C_{ij} = \xi_F(\mathbf{r}_{ij}) + \frac{\langle N_i^2 \rangle}{(C_i \bar{E}_i)^2} \delta_{ij}^K + \xi_c(r_{ij}) \delta^D(\sigma_{ij}) . \quad (3.12)$$

Here,  $\sigma_{ij}$  is the perpendicular component of  $\mathbf{r}_{ij}$ , and the Dirac delta function  $\delta^D$  indicates that the last term is non-zero for pixels on the same quasar spectrum only, as opposed to the Kronecker function  $\delta_{ij}^K$  in the second term that indicates that the noise term is only present when both pixels are the same.

In general, a joint analysis of the Ly $\alpha$  auto-correlation and a cross-correlation may be done, and the measured correlation  $\xi_F$  can then be used to compute the cross-correlation covariance. Here, we use instead a theoretical correlation function computed as the Fourier transform of the Ly $\alpha$  power spectrum measured in [40] from numerical simulations, with modified bias parameters in agreement with the measurement of the correlation function measured with the first year of BOSS data in [13].

We use a Ly $\alpha$  density bias parameter  $b_F = -0.168$  and a redshift distortion parameter  $\beta_F = 1$  at  $z = 2.25$ , and we include the non-linear term  $D(k, \mu_k)$  with the parameter values of the fiducial model in the first row of Table 2 of [40]. These values are consistent with the results of [13]. The amplitude of the correlation function is assumed to be proportional to  $(1+z)^\alpha$ , with  $\alpha = 3.8$ , as found from the 1D power spectrum measurement in [36]. We expect most of the correlated errors in the continuum fitting to be removed by the MTC procedure, so we generally do not include the term  $\xi_c$  in equation (3.12) except when the MTC is omitted. In the latter case, a constant contribution  $\xi_c = 0.03$ , equal to the measured variance of the value of  $\delta_F$  averaged over one spectrum, is added to  $C_{ij}$  for all pixel pairs on a common line of sight.

The calculation of the cross-correlation covariance using equation (3.11) can be time consuming because of the need to evaluate  $\xi_F$  for all pixel pairs with separations within the  $A$  and  $B$  bins from every pair of DLAs. Each sum in the numerator of equation (3.11) is over every DLA, and over every pixel within the separation bin. To increase the speed of the calculation, we include only pixel pairs with a perpendicular separation smaller than  $\sigma_{ij} = 20 h^{-1} \text{ Mpc}$ , a similar approximation to the one used in [13] for computing the covariance matrix. This approach ensures the inclusion of the most important correlations of our Ly $\alpha$  spectra in the covariance matrix.

### 3.5 Sub-samples and bootstrap errors

The errors obtained on the measured cross-correlation using the covariance matrix computed with equations (3.11) and (3.12) rely on the accuracy of this calculation, which may be affected by the assumed Ly $\alpha$  autocorrelation and the neglect of continuum fitting errors and other possible systematics (such as correlated sky subtraction errors). It is therefore useful to compute an alternative set of bootstrap errors by dividing our quasar sample into a number of sub-samples and testing the variation of the obtained cross-correlations among the sub-samples.

We divide the area covered by DR9 into 12 sub-samples as shown in Figure 5. Table 1 provides the number of quasars and the number of DLAs present in each sub-sample. The



DLA- $\text{Ly}\alpha$  cross-correlation and its covariance matrix are separately computed in each sub-sample. The typical sub-sample size is  $\sim 10$  deg, or  $\sim 700 h^{-1}$  Mpc, which is much larger than the maximum scale of our analysis,  $\sigma < 60 h^{-1}$  Mpc. We are therefore not concerned about the loss of a small fraction of DLA- $\text{Ly}\alpha$  pairs that are near the border of two neighboring sub-samples. Because of the geometry of the observed sky area in DR9, most of the sub-samples have short borders with their neighbors.

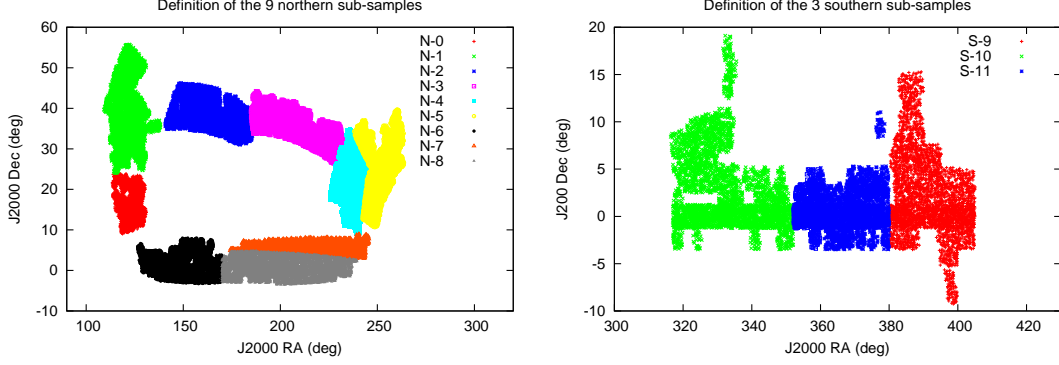


**Figure 5.** The 12 sub-samples in which we split the DR9 quasar sample, 9 in the northern Galactic hemisphere (left) and 3 in the southern one (right).

Sub-sample	# quasars	# DLA
N-0	2290	303
N-1	5176	647
N-2	5264	670
N-3	5246	758
N-4	4010	537
N-5	4056	545
N-6	4823	658
N-7	3255	406
N-8	6322	819
S-9	4339	543
S-10	4308	503
S-11	3360	391

**Table 1.** Number of quasars and DLAs included in our analysis in each of the 12 sub-samples.

The cross-correlations and their covariance matrices are obtained in each sub-sample,  $\hat{\xi}_\alpha$  and  $\tilde{C}_\alpha$ , and are combined using the equations

$$\tilde{C}^{-1} = \sum_{\alpha} \tilde{C}_{\alpha}^{-1} , \quad (3.13)$$

$$\hat{\xi} = \tilde{C} \sum_{\alpha} \tilde{C}_{\alpha}^{-1} \hat{\xi}_{\alpha} . \quad (3.14)$$

Bootstrap errors are calculated from these 12 sub-samples by generating  $N = 100$  random combinations of the 12 sub-samples with repetitions, and recomputing  $\tilde{C}$  and  $\hat{\xi}$  for

each of these 100 combinations [41]. The dispersion among these combinations of the values of any model parameter that is fitted to the result yields the bootstrap error.

### 3.6 Fitting the DLA bias

In the limit of large-scales, linear theory predicts the precise form of all the correlations among any pair of tracers of the large-scale structure in redshift space. The Ly $\alpha$  forest probes material at low density and high redshift, which is less affected by non-linear evolution and random peculiar velocities than a set of galaxies moving on orbits within gravitationally collapsed halos. Therefore, linear theory remains a good approximation down to smaller scales for the Ly $\alpha$  forest than for other tracers. In linear theory, redshift distortions cause the amplitude of each Fourier mode in a biased tracer field to be enhanced by the factor  $b(1 + \beta\mu_k^2)$ , where  $b$  is the density bias factor,  $\beta$  is the redshift distortion parameter, and  $\mu_k$  is the cosine of the angle between the Fourier mode and the line of sight [42]. The linear cross-power spectrum of the DLAs and the Ly $\alpha$  forest is therefore equal to

$$P_{DF}(\mathbf{k}, z) = b_D(z) [1 + \beta_D(z)\mu_k^2] b_F(z) [1 + \beta_F(z)\mu_k^2] P_L(k, z) . \quad (3.15)$$

where  $b_D$  and  $b_F$  are the DLA and Ly $\alpha$  density bias factors,  $\beta_D$  and  $\beta_F$  are their redshift space distortion parameters, and  $P_L(k, z)$  is the linear matter power spectrum. The cross-correlation function is the Fourier transform of  $P_{DF}$ , and can be computed using the following equations (derived as in [43])

$$\xi(\mathbf{r}) = \xi_0(r)P_0(\mu) + \xi_2(r)P_2(\mu) + \xi_4(r)P_4(\mu) , \quad (3.16)$$

where  $\mu = \pi/r$  is the angle cosine in redshift space,  $P_0$ ,  $P_2$  and  $P_4$  are the Legendre polynomials, and the functions  $\xi_0$ ,  $\xi_2$  and  $\xi_4$  are

$$\xi_0(r) = b_D b_F [1 + (\beta_D + \beta_F)/3 + \beta_D \beta_F/5] \zeta(r) , \quad (3.17)$$

$$\xi_2(r) = b_D b_F [2/3(\beta_D + \beta_F) + 4/7\beta_D \beta_F] [\zeta(r) - \bar{\zeta}(r)] , \quad (3.18)$$

$$\xi_4(r) = 8/35 b_D b_F \beta_D \beta_F [\zeta(r) + 5/2\bar{\zeta}(r) - 7/2\bar{\bar{\zeta}}(r)] . \quad (3.19)$$

The function  $\zeta(r)$  is the linear correlation function in real space, and  $\bar{\zeta}(r)$  and  $\bar{\bar{\zeta}}(r)$  are averages of  $\zeta(r)$  within  $r$  given in equation (9) of [43]. We compute  $\zeta(r)$  using the  $\Lambda$ CDM model with the parameters given at the end of the Introduction.

We assume the DLA bias  $b_D$  to be constant with redshift, while for the Ly $\alpha$  forest, we assume the bias evolves as  $b_F(z)/b_F(z = 2.25) = [(1+z)/3.25]^{\alpha/2+1}$ , where  $\alpha = 3.8$  describes the evolution of the amplitude of the line-of-sight power spectrum measured in [36]. The rapid evolution of the amplitude of  $\delta_F$  in the Ly $\alpha$  forest is a consequence of the rapid change in the mean transmitted fraction with redshift.

For the redshift distortion of the DLAs, we assume  $\beta_D = f(\Omega)/b_D \approx b_D^{-1}$ , where  $f(\Omega)$  is the logarithmic derivative of the linear growth factor [42], which is close to unity at  $z > 2$  in the  $\Lambda$ CDM model. This assumption may not be exactly correct for DLAs if the probability of detection of a DLA depends on the large-scale peculiar velocity gradient because of the Ly $\alpha$  forest absorption that is superposed on the damped wings. This effect would generate

a peculiar velocity bias analogously to the case of the Ly $\alpha$  forest, but we expect this effect to be small.

For the Ly $\alpha$  forest,  $b_F$  and  $\beta_F$  are independent because the  $\delta_F$  tracer is subject to a strong bias by the large-scale peculiar velocity gradient [40]. We use the results for the Ly $\alpha$  autocorrelation of [13] to fix  $b_F(1 + \beta_F) = -0.336$ . Most of our results will be presented assuming  $\beta_F = 1.0$ , in which case the only free parameter is  $b_D$ . Some results will also be obtained when  $\beta_F$ , which was poorly determined by [13], is also treated as a free parameter. Note that the Ly $\alpha$  forest has a negative bias, since denser regions of the universe have a lower transmitted flux. This implies that the cross-correlation is also negative.

The model of the linear theory in equation (3.16) is generally modified to account for the effect of the MTC, which removes the mean value of  $\delta_F$  in each quasar spectrum, therefore distorting the DLA-Ly $\alpha$  cross-correlation. The way this correction is modeled and calculated is explained in Appendix A. Instead of evaluating the theoretical model at the center of every bin in the  $\sigma, \pi$  components of the DLA-Ly $\alpha$  separation, we evaluate it at the weighted average values of  $\sigma, \pi$  for all the DLA-Ly $\alpha$  pairs that contribute to the bin. To minimize possible non-linear effects on the correlation function, all the fits are done using only bins with  $r > 5 h^{-1}$  Mpc; this eliminates the two bins with smallest  $\sigma$  and  $\pi$ , reducing the number of bins to 126.

For each theoretical model that predicts the cross-correlation at each bin  $A$  of  $(\pi, \sigma)$ ,  $\xi_{t,A}$ , we compute its  $\chi^2$  as

$$\chi^2 = (\hat{\xi}_A - \xi_{t,A}) \tilde{C}_{AB}^{-1} (\hat{\xi}_B - \xi_{t,B}) , \quad (3.20)$$

where the indexes  $A$  and  $B$  are summed over all bins. The likelihood function is

$$L = \frac{\exp[-0.5 \chi^2]}{(2\pi)^{N/2} |\tilde{C}|} , \quad (3.21)$$

where  $|\tilde{C}|$  is the determinant of the covariance matrix of the cross-correlation (computed using equations 3.11 and 3.13),  $N = 126$  is the number of bins, and we have assumed that the distribution of errors in the cross-correlation is Gaussian.

Our best estimate of the DLA bias is the one that maximizes the likelihood, and its uncertainty is evaluated using two different approaches. First we estimate the errors on the fitted parameters with the Monte Carlo Markov Chain technique (MCMC errors), where we sample the parameter space using the likelihood function described above and compute the dispersion around the best fit value. Secondly, the fits are repeated with the bootstrap realizations of the 12 sub-samples randomly selected with repetitions as described previously, obtaining the bootstrap error (BS error) from the dispersion in the fitted parameters among the bootstrap realizations. Both the MCMC and BS errors will be presented.

## 4 Results

In this section the results of the cross-correlation of DLAs and the Ly $\alpha$  absorption in redshift space are presented. After obtaining a fit to our fiducial model with only one free parameter, the bias factor of DLAs, we analyze the consistency of the covariance matrix and the bootstrap

errors, the evidence for the presence of redshift distortions, and the dependence of our best fit model on the range of separations that are used. We then investigate a variety of possible dependences of the DLA bias factor on several variables: redshift, column density, and the Ly $\alpha$  forest redshift distortion parameter. In general the results presented here have been corrected with the MTC, and the fitted models are also corrected as described in Appendix A, except when we test for the effect of the MTC.

#### 4.1 Measured cross-correlation and bias parameter

The results of the cross-correlation as a function of  $\pi$  for our fiducial model are shown as red points with errorbars in figures 6 and 7 in eight panels, corresponding to our eight bins in  $\sigma$ . The errorbars are the square root of the diagonal elements of the covariance matrix  $\tilde{C}$  computed as described in section 3.4 (equation 3.13). The blue solid curves are our best fit fiducial model (all of our fits exclude bins at  $r = (\sigma^2 + \pi^2)^{1/2} < 5 h^{-1} \text{Mpc}$ , which are only the two bins at the lowest  $\sigma$  and  $\pi$ , even though they are shown in the figures), which fixes  $\beta_F = 1$  and fits only one free parameter, the DLA bias. The result obtained from our covariance matrix is  $b_D = 2.17 \pm 0.20$ , with a  $\chi^2$  of 106 for 125 degrees of freedom, and the bootstrap analysis gives the same errorbar. Note that we are measuring only the amplitude of the cross-correlation, which is proportional to  $b_D b_F \sigma_8^2$  and depends on  $\beta_F$ , and the error on  $b_D$  here reflects only that in our measurement of the amplitude. The results are also shown in a contour plot in the left panel of figure 8, and the best fit fiducial model is shown in the right panel with the same contour levels.

As seen in the figures and indicated by the  $\chi^2$  value, the fit of the standard  $\Lambda\text{CDM}$  model to the DLA-Ly $\alpha$  forest cross-correlation is excellent. The measurements are fully consistent with the radial dependence and anisotropy that is expected in linear theory for the model that agrees with all other cosmological determinations of the large-scale power spectrum.

#### 4.2 Effect of the MTC

All our results are generally obtained including the MTC, and the fitted models include the correction described in Appendix A. We now check the effect of the MTC by recomputing the cross-correlation without including the correction, i.e., by using directly the PCA-only continuum. In this case, we add to our covariance matrix the additional term  $\xi_c = 0.03$  in equation (3.12) due to the error of the continuum fitting for pixels on a common line of sight.

The measurements with and without the MTC are compared in figure 9 (red and black errorbars), for four selected  $\sigma$  bins. The best fit model is also shown with and without including the correction of appendix A (blue solid and dotted green line, respectively). Table 2 shows the result for the bias for the NOMTC case (uncorrected data and uncorrected fit model), and for the case where we apply the MTC to the data but we leave the fitted model uncorrected (NOCOR case).

The effect of the MTC is clearly a minor one; it has little effect on the result on the DLA bias, and the errorbars are only increased by  $\sim 10\%$  when the continuum fitting errors are included. The effect of the correction of appendix A is small compared to the present errorbars of the measurements, but our model characterization of the effect of the MTC is supported by the larger value of  $\chi^2$  in the NOCOR case. We keep the correction despite

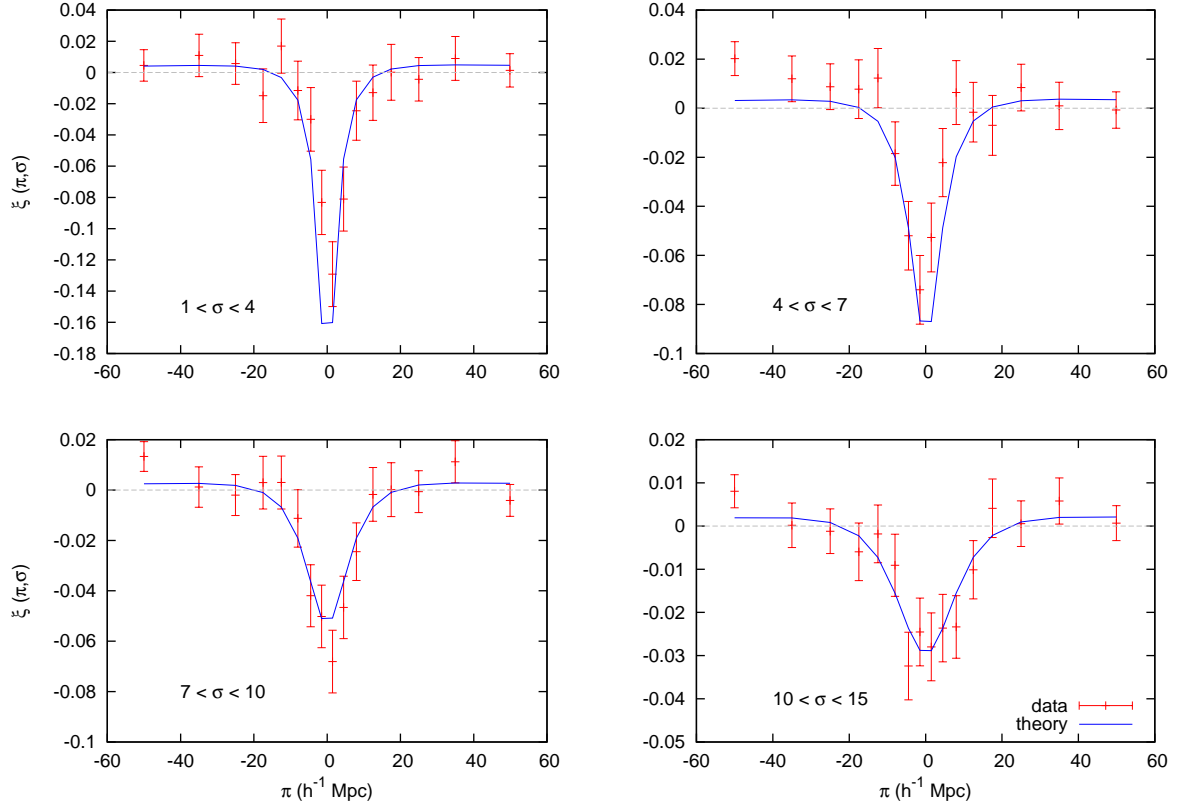


**Figure 6.** Measured cross-correlation in different bins of  $\sigma$ : from top-left to bottom-right,  $1 < \sigma < 4 h^{-1} \text{ Mpc}$ ,  $4 < \sigma < 7 h^{-1} \text{ Mpc}$ ,  $7 < \sigma < 10 h^{-1} \text{ Mpc}$ , and  $10 < \sigma < 15 h^{-1} \text{ Mpc}$ . Solid lines show the best fit model for the fiducial analysis, including the correction derived in appendix A.

	$b_D$	BS errors	MCMC errors	$\chi^2$ (d.o.f)
FIDUCIAL	2.17	0.20	0.20	106 (125)
NOMTC	2.11	0.21	0.22	109 (125)
NOCOR	2.00	0.19	0.20	111 (125)
NODLA	2.25	0.22	0.21	109 (125)
LOWZ ( $2 < z < 2.25$ )	2.18	0.41	0.33	116 (125)
MIDZ ( $2.25 < z < 2.5$ )	2.16	0.32	0.34	109 (125)
HIGHZ ( $2.5 < z < 3.5$ )	1.88	0.57	0.37	92 (125)
LOWNHI ( $\log(N_{HI}) < 20.4$ )	2.27	0.30	0.29	133 (125)
HIGHNHI ( $\log(N_{HI}) > 20.4$ )	1.89	0.26	0.30	110 (125)

**Table 2.** Best fit value of the DLA bias with its bootstrap errors, MCMC errors and  $\chi^2$  value of the fit, for various analyses: FIDUCIAL (with the MTC and the theory corrected with the expression derived in appendix A), NOMTC (PCA-only continuum fitting, uncorrected theory), NOCOR (MTC, uncorrected theory), NODLA (spectra containing DLAs are rejected), data split in redshift bins (LOWZ, MIDZ, HIGHZ) and finally the DLA sample split in two bins of column density (LOWNHI, HIGHNHI).

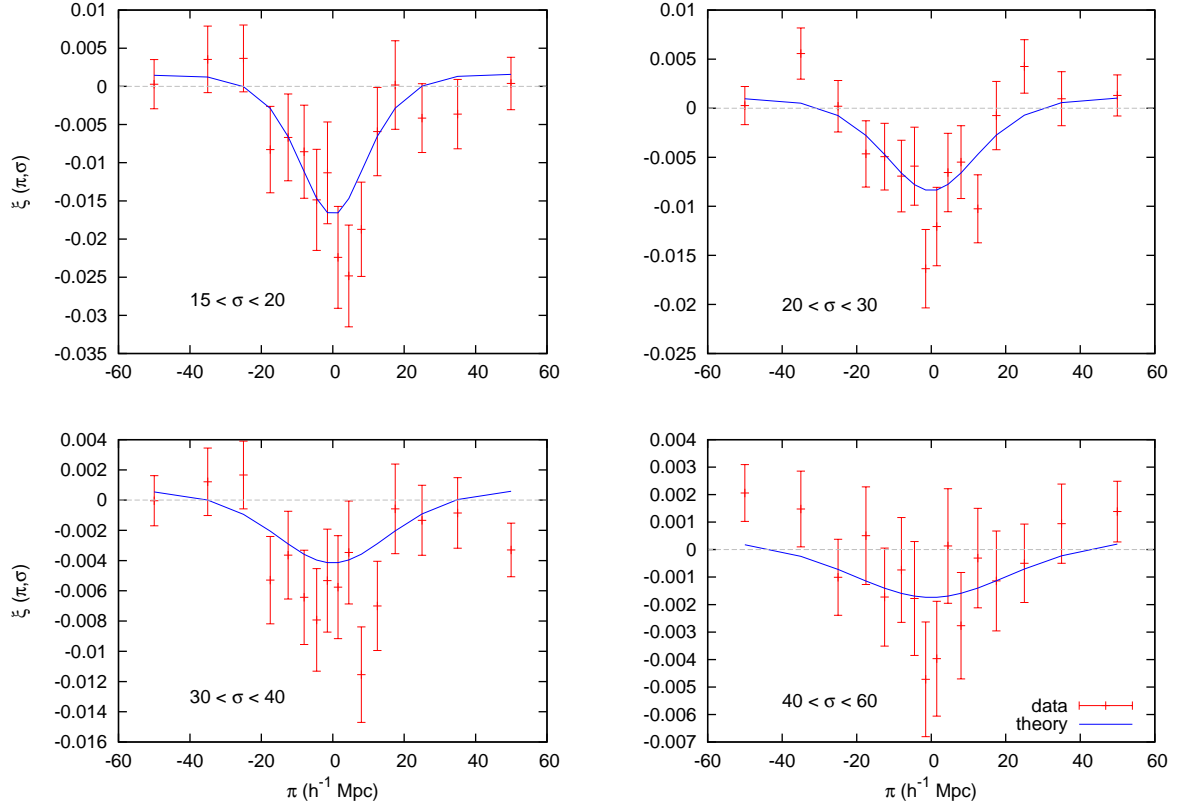


**Figure 7.** Same as figure 6, for the  $\sigma$  bins, from top-left to bottom-right,  $15 < \sigma < 20 h^{-1} \text{ Mpc}$ ,  $20 < \sigma < 30 h^{-1} \text{ Mpc}$ ,  $30 < \sigma < 40 h^{-1} \text{ Mpc}$ , and  $40 < \sigma < 60 h^{-1} \text{ Mpc}$ .

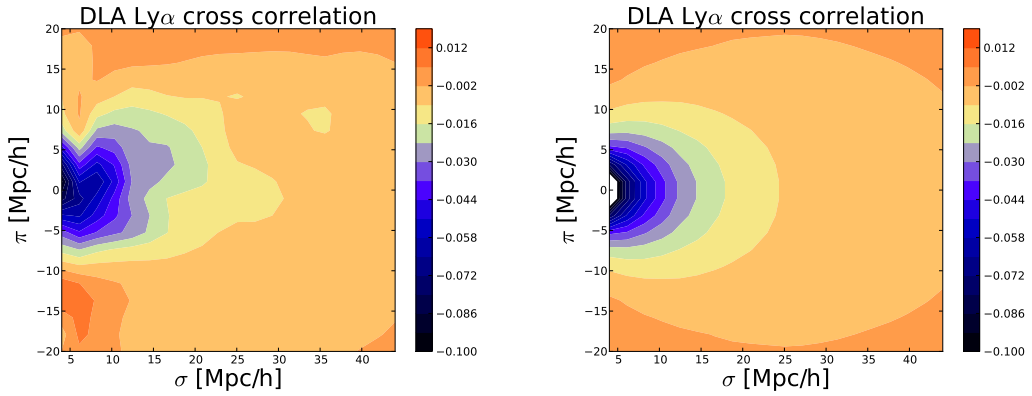


**Figure 8.** Contour plot of the measured redshift space cross-correlation for our fiducial analysis (left) and our best fit theoretical model that includes the MTC correction (right).

the fact that with the present level of noise its effect is not significant, because it will be important for future studies with smaller errorbars and larger separations.

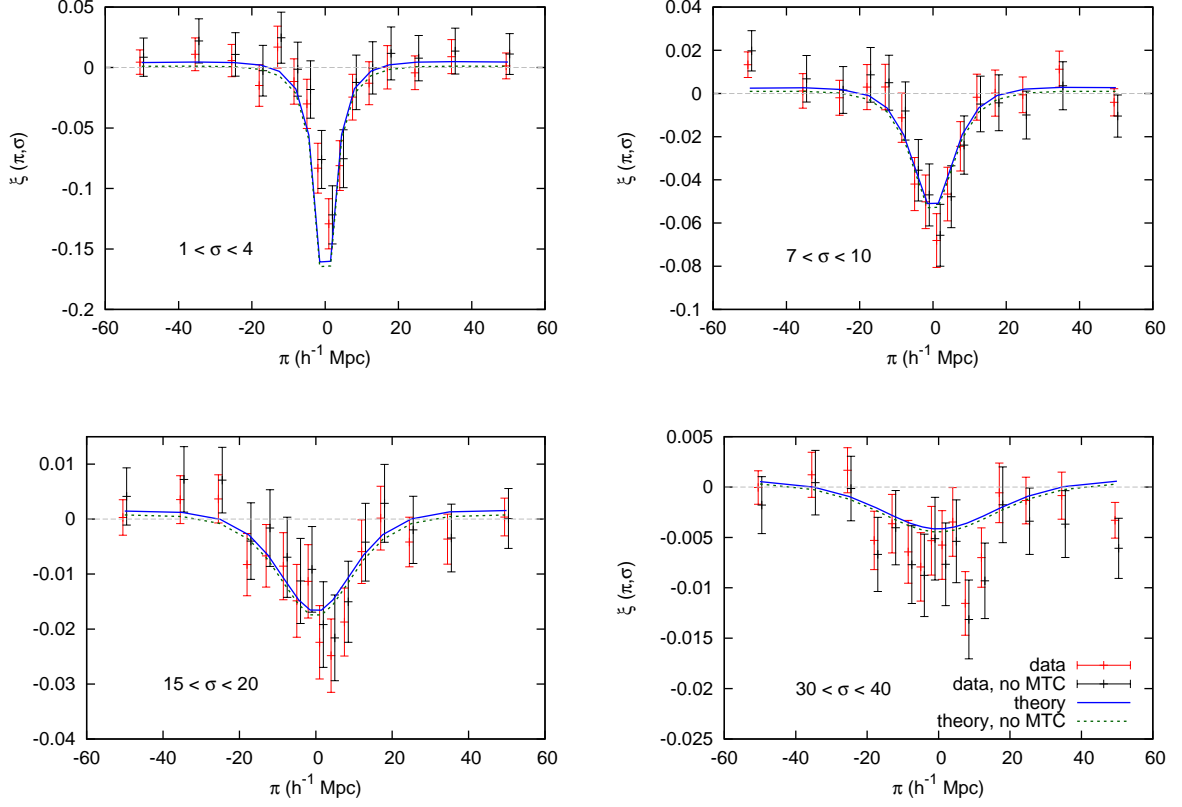


**Figure 9.** Effect of the MTC on the measured cross-correlation in the four selected bins of  $\sigma$  that are indicated. The fiducial measurement is plotted with red errorbars, while the measurement without the MTC is shown in black (with a small horizontal shift for better visualization). The blue solid line is the fiducial theory including the MTC from appendix A, and the dotted green line without the MTC.

### 4.3 Tests of the covariance matrix

We have seen that the bootstrap error on the fitted bias parameter of the DLAs is generally in good agreement with the one computed from our covariance matrix using the MCMC technique (see table 2). As a further test of the accuracy of our errors, we now compare the scatter between the values of the measured cross-correlation in bins, using the 12 sub-samples defined in section 3.5, with the predicted errors from the diagonal elements of the covariance matrix.

For the purpose of this comparison, instead of averaging the cross-correlation values from the sub-samples weighted with their inverse covariance matrices, as in equation 3.14, we average by weighting each sub-sample with the sum of the weights of all the pixels that contributed to each bin  $A$ ,  $\tilde{w}_A^\alpha$ , where the index  $\alpha$  labels each sub-sample. This estimate of the cross-correlation in bin  $A$  is

$$\hat{\xi}_A = \frac{\sum_{\alpha} \hat{\xi}_A^{\alpha} \tilde{w}_A^{\alpha}}{\sum_{\alpha} \tilde{w}_A^{\alpha}}. \quad (4.1)$$

and the uncertainty  $\sigma_A$  of this estimate is

$$\sigma_A^2 = \frac{1}{(\sum_{\alpha} \tilde{w}_A^{\alpha})^2} \sum_{\alpha} (\tilde{w}_A^{\alpha})^2 \left[ (\hat{\xi}_A^{\alpha})^2 - (\hat{\xi}_A)^2 \right]. \quad (4.2)$$

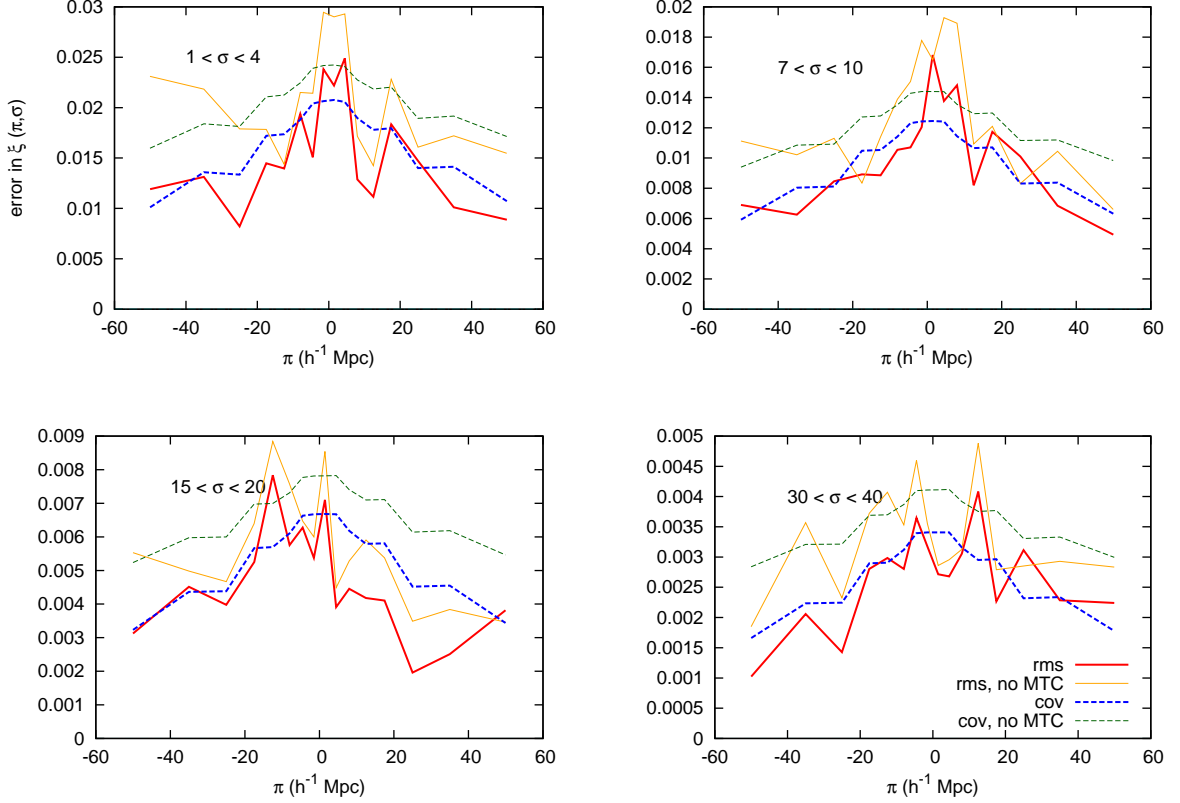


**Figure 10.** Errors of the cross-correlation in four selected bins of  $\sigma$ , as indicated in each panel. The solid lines show the estimate from the scatter between sub-samples (equation 4.2), while the dashed lines show the estimate from the diagonal elements of the covariance matrix.

In figure 10 the errors computed from the scattering among the sub-samples and from the diagonal elements of the covariance matrix are compared. The errors from the scatter among sub-samples (solid lines) are noisy because of the small number of sub-samples, but in general they agree remarkably well with the ones obtained from the covariance matrix (dashed lines). The thick lines are for the fiducial case, and the thin lines for the NOMTC case. As before, the NOMTC case incorporates continuum fitting errors that account for the larger covariance errors by  $\sim 10\%$ . Generally the NOMTC case has larger scatter than the MTC case, as we would expect if the MTC actually helps reducing the uncertainty in the cross-correlation measurement.

#### 4.4 Evidence for the redshift distortions

The gravitational evolution origin of the DLA- $\text{Ly}\alpha$  absorption cross-correlation we detect is tested by the presence of the predicted redshift distortions in linear theory. The expected



elongation of contours perpendicular to the line of sight is apparent in figure 8. By fitting only the DLA bias factor and making the reasonable choice  $\beta_F = 1$  based on previous observations of the Ly $\alpha$  autocorrelation in [13], the observed anisotropy is consistently matched by our linear model. The detection of redshift distortions can be quantified by comparing with a fit that forces isotropy requiring  $\beta_F = \beta_D = 0$ . This isotropic fit yields  $\chi^2 = 150$ , implying a detection of more than  $6\sigma$  when compared to  $\chi^2 = 106$  (125 d.o.f.) for our best fit model with  $\beta_F = 1$  and  $\beta_D = f(\Omega)/b_D$  (points at  $r < 5 h^{-1}$  Mpc are not used in the fits in both cases). This result provides strong support for the interpretation that the measured cross-correlation is induced by the gravitational growth of large-scale structure that is traced by the DLAs and the Ly $\alpha$  forest.

#### 4.5 Scale dependence of the DLA bias

In addition to the redshift distortions, the predicted dependence of the cross-correlation on the separation  $r$  in the  $\Lambda$ CDM model is another important test that our measurement agrees with the theoretical expectation. This can be rephrased as testing that the inferred DLA bias factor is constant in different intervals of  $r$ . The results of this exercise are shown in figure 11.

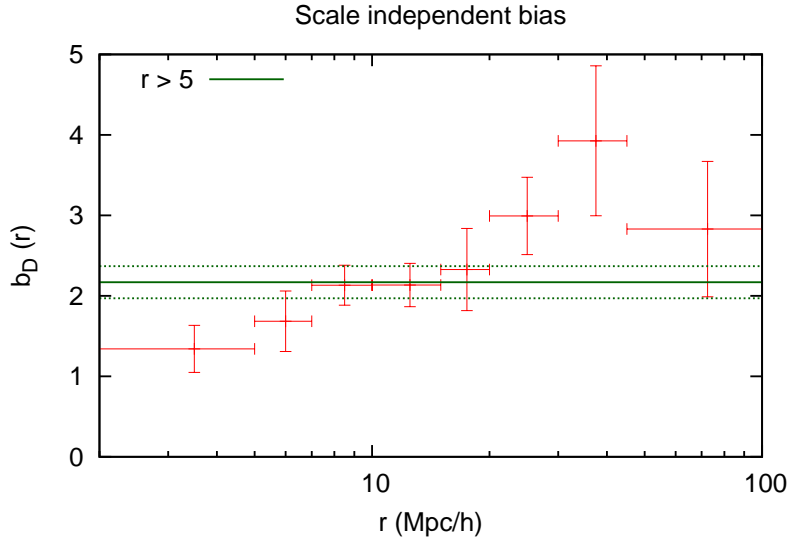


**Figure 11.** Fitted DLA bias in several bins of the separation  $r$  for our fiducial analysis. The green lines show the values obtained when combining all bins above  $r > 5 h^{-1}$  Mpc.

The value of the bias is consistent with being constant for  $r > 5 h^{-1}$  Mpc. At smaller scales we expect non-linear effects to be important, so it is not surprising that the first point has a discrepant value of the bias. The first bin that we use in our fits,  $5 h^{-1}$  Mpc  $< r < 7 h^{-1}$  Mpc, also has a lower bias than the ones at larger radii by  $1.3\sigma$ , and it may already be affected by non-linear effects to some degree. In addition to the physical non-linearities in the distribution of gas and DLAs in redshift space, the transformation from optical depth to the transmitted fraction introduces an additional non-linearity that in this case may be the dominant effect.

The presence of non-linearities may be accounted for in the future by using predictions from hydrodynamic numerical simulations of structure formation. When the full BOSS dataset is available, the reduced error bars will allow for a better measurement of these non-linear effects. We have also checked the symmetry of the cross-correlation under a sign change of the  $\pi$  coordinate. There is no statistically significant difference between the fitted fiducial model when only the bins with  $\pi > 0$  or those with  $\pi < 0$  are used.

#### 4.6 Effect of the DLAs on the Ly $\alpha$ forest

In our fiducial analysis we include in the Ly $\alpha$  sample 3047 lines of sight that contain at least one DLA. As explained in section 2, we apply a mask on the central region of the absorption profiles and correct for the damped wings by multiplying the continuum estimate with a Voigt profile. To test the effect of this correction we measure the cross-correlation using only the remaining 49402 lines of sight. The results can be seen in table 2 under the name NODLA, and are clearly consistent with our fiducial analysis.

#### 4.7 Dependence on the Ly $\alpha$ bias

Our fits for the DLA bias are based on assuming fixed values for the Ly $\alpha$  forest bias parameters: the well constrained combination  $b_F(1 + \beta_F) = -0.336$  from [13], and  $\beta_F = 1$ . The value of  $\beta_F$  is still highly uncertain, but improved measurements are expected in the near future from BOSS. We therefore examine the dependence of our result for  $b_D$  on the assumed value of  $\beta_F$ .

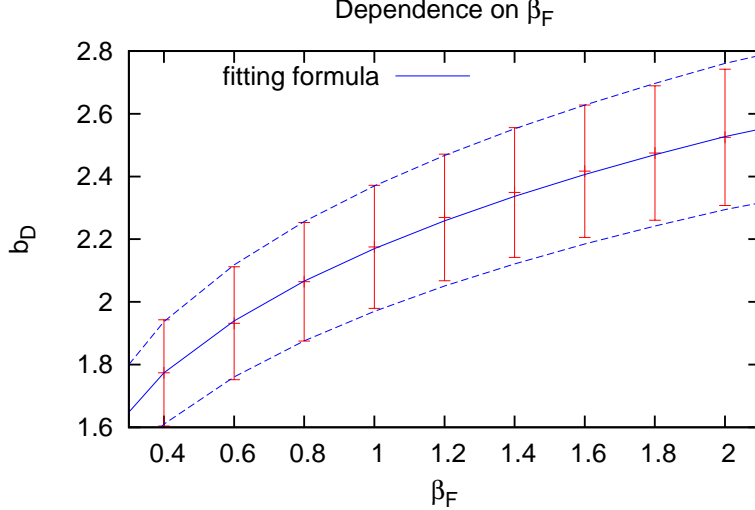


**Figure 12.** Best fit value of the DLA bias for different values of  $\beta_F$ , for our fiducial analysis. The dependence is well described with the fitting formula  $b_D = (2.17 \pm 0.2)\beta_F^{0.22}$  (blue line).

In figure 12 we plot the results assuming different values of  $\beta_F$ . We show that for the most plausible range  $0.4 < \beta_F < 2.0$ , the dependence is well fitted by a simple function

$$b_D = (2.17 \pm 0.20) \beta_F^{0.22} . \quad (4.3)$$

Figure 13 shows the likelihood contours for the two-parameter fit when  $b_F$  is allowed to vary, keeping fixed the combination  $b_F(1 + \beta_F) = -0.336$ , for our fiducial analysis. The data clearly prefer larger values of  $\beta_F$  (smaller values of  $b_F$ ) than the one we have assumed so far ( $\beta_F = 1$ ,  $b_F = -0.168$ ). However, the best fit value of  $\beta_F$  is quite sensitive to the applied correction, and so we prefer to be conservative by assuming a fixed, low value of  $\beta_F$ , minimizing the required value of the DLA bias.

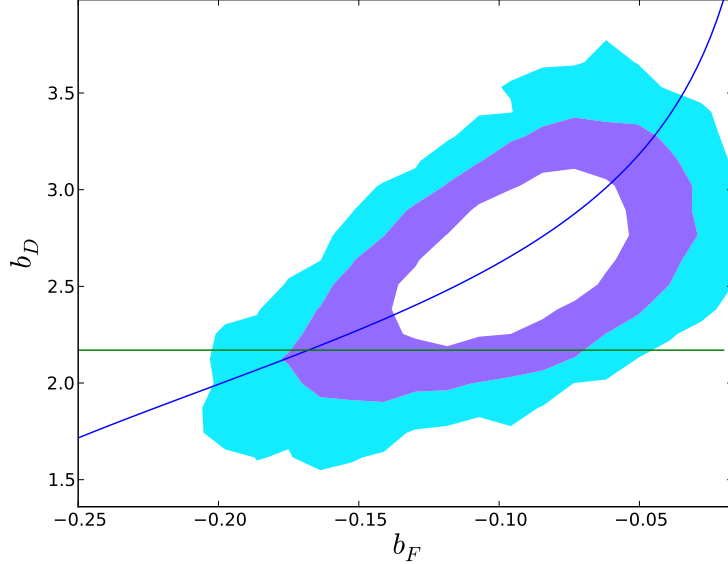


**Figure 13.** Degeneracy between the value of  $b_D$  and  $b_F$  when fitting both parameters at the same time in our fiducial analysis. Since we keep fixed the well constrained quantity  $b_F(1 + \beta_F) = -0.336$ , each value of  $b_F$  is related to a value of  $\beta_F$ . The horizontal green line shows the best fit value when fixing  $\beta_F = 1$  ( $b_F = -0.168$ ),  $b_D = 2.17$ . The blue line shows the fitted function in equation 4.3.

#### 4.8 Redshift evolution

Until now we have assumed that the value of the DLA bias is constant with redshift. We now evaluate the cross-correlation in three different redshift bins,  $2.0 < z < 2.25$  (LOWZ),  $2.25 < z < 2.5$  (MIDZ) and  $2.5 < z < 3.5$  (HIGHZ). The third bin is wider because the Ly $\alpha$  forest data available for cross-correlation is much more sparse at high redshift in BOSS. We assume the redshift evolution of the Ly $\alpha$  forest bias factor to be  $b_F \propto (1 + z)^{2.9}$ , based on the evolution of the line of sight power spectrum measured in [36]. The best fit values for the three redshift bins, shown in table 2, provide some evidence that the DLA bias decreases with redshift. This evolution is opposite to that expected if the DLA host halos are approximately at constant velocity dispersion: in this case the DLA bias should increase with redshift as the host halos become increasingly rare fluctuations. The observed trend is, however, of low statistical significance.

## 4.9 Dependence on column density

Finally, we split our sample of DLAs into two data sets as a function of column density, separated at  $N_{HI} = 10^{20.4} \text{ cm}^{-2}$ . If systems with higher column density resided in halos of higher mass, one would expect the bias of the high column density sub-sample (HIGHNHI) to be larger than that of the low column density (LOWNHI). The results shown in table 2 are consistent with a bias that is independent of column density, showing, if anything, an opposite trend that is not statistically significant.

A possible systematic error that may affect our DLA bias is the inclusion in our DLA catalogue of systems that are not actual DLAs, but regions of absorption with lower column density than our threshold which pass our column density cut because of a combination of spectral noise and the Ly $\alpha$  forest superposed on the damped wings. At the same time, DLAs that are just above our column density cut may more easily be attributed a column density below the threshold (and be therefore omitted from the catalogue) when the superposed Ly $\alpha$  forest is particularly weak. If this error is important, the Ly $\alpha$  forest superposed on the wings of DLAs may introduce a correlation with the Ly $\alpha$  forest in nearby lines of sight that would systematically enhance our measured  $b_D$ . We do not believe this effect is important because preliminary tests of the DLA selection with mocks show that there is a low rate of miss-identifications ([26]), and because of the consistency of the radial dependence of the cross-correlation and the anisotropy with theoretical expectations found in sections 4.4 and 4.5, but we plan to examine this selection effect more carefully in the future using the techniques described in [39].

## 4.10 Result for the sample affected by BAL Contamination

As seen in figure 1, there is a significant excess of systems detected in the window  $1005 \text{ \AA} \leq \lambda_r \leq 1037 \text{ \AA}$ , probably due to contamination by BALs with small Balnicity index  $BI$ . The systems detected in this window were rejected in the fiducial analysis. We measured the cross-correlation using only the 989 systems that fall into this range of restframe wavelength, including those detected in lines of sight with a Balnicity index in the range  $0 < BI < 1000 \text{ km s}^{-1}$ . The measured bias is  $b_D = 0.68 \pm 0.50$  (BS errors), showing that at least half of these systems are indeed contaminants, and confirming that the measured cross-correlation is present only for physically real DLAs.

## 5 Discussion

The measurement of the cross-correlation of DLAs and the Ly $\alpha$  forest absorption, presented for the first time in this paper, provides a new observational constraint on the nature of DLAs: the bias factor of their host halos. We have measured this bias factor to be  $b_D = (2.17 \pm 0.20)\beta_F^{0.22}$ , at a mean redshift of  $z = 2.3$ . The analysis of numerical simulations of the Ly $\alpha$  forest predict a value of  $\beta_F \simeq 1.5$  ([40]), and even though the first measurement of  $\beta_F$  from the Ly $\alpha$  forest autocorrelation [13] allowed for a wide range of  $\beta_F$  around unity, a more recent analysis also suggests a value larger than one (Slosar, private communication).

As discussed in the introduction, the bias factor constrains the mass distribution of the host halos of DLAs. A small bias factor implies low halo masses and an association of most

DLAs with dwarf galaxies, while a large bias factor means that most DLAs are extended clouds in massive halos. The observational determination of the mean bias factor is therefore a new constraint that models of DLAs must satisfy.

Theoretical models of DLAs need to provide the average cross section of a halo of mass  $M$  for producing an absorption system with  $N_{HI} > 10^{20.3} \text{ cm}^{-2}$ . The predicted rate of incidence is given by equation (1.1), and the new observable of the mean bias factor to be matched by models is obtained with equation (1.2). Numerical simulations of galaxy formation following the collapse and radiative cooling of gas in halos have found that the rate of incidence predicted for DLAs is affected by two uncertain factors: the limited resolution of the simulations and the impact of galactic winds ([44], [45], [46]). As the resolution is improved and halos are well resolved down to the lowest masses for which photoionized gas can collapse, the rate of incidence is increased; at the same time, when a prescription for supernova-driven galactic winds is included leading to the ejection of gas from low-mass halos when star formation occurs, the gas mass and the DLA cross sections in low-mass halos decrease as the energy that is deposited in winds is increased ([47],[48], [49], [50]).

These models based on cosmological simulations do not at present provide fundamental physical predictions for the properties of DLAs, because the way that the gas distribution in halos is affected by cooling and fragmentation, radiative transfer, star formation and galactic winds depends on extremely complex physical processes that can only be roughly approximated through simple parameterized recipes that are incorporated into the equations being solved in the simulations. Nevertheless, they can provide a basic guide as to the general characteristics of star formation rates and wind strengths that are needed to satisfy the observational constraints.

### 5.1 Constraints on the halo mass distribution from the bias factor

We now examine the expected bias factors for simple relations of the DLA cross section and the halo mass that are useful fits to the results found in the numerical simulations of DLAs. The DLA systems are likely distributed over a wide range of halo mass, but they are not expected in halos that are too shallow to hold photoionized gas and allow it to radiatively cool. This condition corresponds to a halo circular velocity of  $v_c \sim 20 \text{ km s}^{-1}$ , or a halo mass at  $z = 2.3$   $M_h \sim v_c^3 / (3\pi H G) \sim 10^9 M_\odot$ . Many numerical models of DLAs, starting with [45], have obtained fits to simulation results with a power-law relation for the cross section,

$$\Sigma(M) = \Sigma_0 (M/M_{min})^\alpha \quad (M > M_{min}) . \quad (5.1)$$

The distribution of halo masses and the bias factor of halos has been thoroughly examined in analytic models and numerical simulations and are robustly predicted in the  $\Lambda$ CDM model (e.g., [6]; [7]). Here we use the mass distribution and halo-bias relation given by [7].

In the left panel of figure 14, the halo mass-bias relation of [7] is shown as the solid purple line. The other lines show the average value of the bias weighted according to the power-law cross section of equation (5.1), for several values of  $\alpha$ , as a function of  $M_{min}$ . All the relations are computed at  $z = 2.3$ , the mean redshift of our DLA bias measurement. Halos having the value of the mean bias we have measured for DLAs have masses of  $\sim 6 \times 10^{11} M_\odot$  (we use  $h = 0.71$ ). Realistically, the host halo masses should vary over a broad range, but

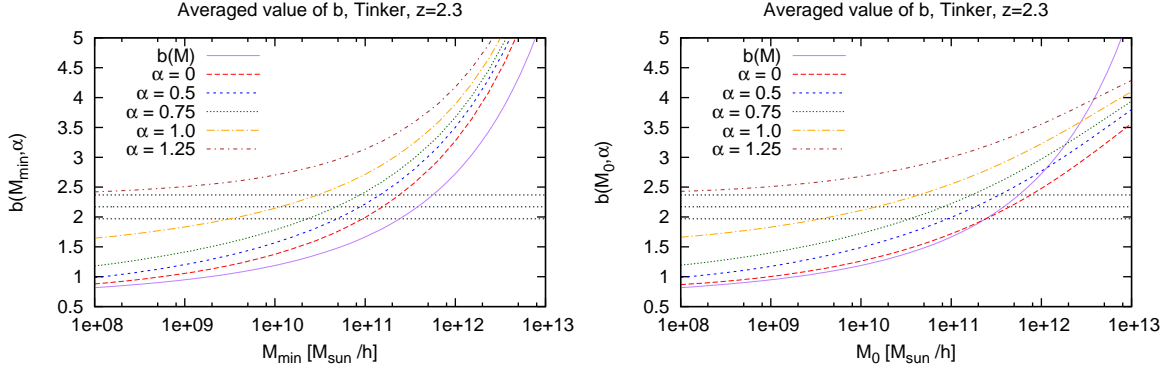


**Figure 14.** Average bias as a function of  $M_{min}$  when the cross section depends on halo mass as  $M_h^\alpha$  with a sharp lower limit at  $M_{min}$  (left), and for the model of equation (5.2) with a smooth suppression at masses below  $M_0$ , for several values of  $\alpha$ , computed at  $z = 2.3$  using [7]. The horizontal dotted lines show the result of this paper for the mean DLA bias with  $1\sigma$  errorbars.

this mass should be a typical one. Our measurement of the bias factor clearly requires DLAs to be mostly associated with host halos of relatively massive galaxies.

Fixing the lower limit in equation (5.1) at  $M_{min} \simeq 10^9 M_\odot$ , the best value of  $\alpha$  that fits our measured bias for  $\beta_F = 1$  is  $\alpha = 1.1 \pm 0.1$ . To better interpret the implication of this result, consider a simple model where the DLAs are clouds found within a fixed fraction  $f_a$  of the virial radius of the halo,  $r_{vir} \propto M^{1/3}$ , with a covering factor  $f_c$ . Then the cross section of a halo is  $\Sigma(M) \propto f_a^2 f_c M^{2/3}$ . In other words,  $\alpha = 2/3$  if DLAs are found within a fixed fraction of the virial radius and have a constant covering factor. This value of  $\alpha$  is ruled out by our result at the  $4\sigma$  level for  $M_{min} = 10^9 M_\odot$ . Therefore, DLAs must cover an increasing fraction of the projected area of halos with increasing mass, up to masses larger than  $\sim 10^{12} M_\odot$ . For  $\beta_F = 0.6$ ,  $\alpha = 2/3$  is still ruled out at the  $3\sigma$  level.

Most of the models from cosmological simulations predict shallower slopes than are implied by our result of the DLA bias. Models without strong effects from galactic winds predict a slope close to  $\alpha = 2/3$  (see, e.g., [48], [50], [51], [52], [53] for recent work on the effects of galactic winds and differences among hydrodynamic codes). Models with the strongest winds are barely consistent with our measured bias factor: model Q5 of [47],[48], with  $\alpha = 1$  and  $M_{min} \simeq 10^9 M_\odot$ , yields a bias about  $1.5\sigma$  below our measurement. The model of momentum-driven winds of [51], with  $\alpha = 0.92$  at  $z = 2.25$ , is also barely consistent.

The right panel in figure 14 shows the same relation of the mean bias for a model where the sharp cutoff of the cross section at  $M_{min}$  is replaced by a smooth function:

$$\Sigma(M) = \Sigma_0 \left( \frac{M}{M_0} \right)^2 \left( 1 + \frac{M}{M_0} \right)^{\alpha-2}. \quad (5.2)$$

We find that the numerical results of [50] (see their figure 4) are well matched by this formula with  $\alpha = 0.5$ ,  $M_0 = 10^{9.5} M_\odot$ , and  $\Sigma_0 = 40 \text{ kpc}^2$ . Their results are at  $z = 3$ ; to shift them to  $z = 2.3$  we assume that the properties of DLAs stay constant in halos of fixed circular velocity, which shifts their characteristic halo mass to  $M_0 = 10^{9.7} M_\odot$ . Their model predicts

a mean bias factor  $b_D \simeq 1.35$ , which is ruled out by our measurement at more than the  $3\sigma$  level if  $\beta_F > 1$ . Even if  $\beta_F = 0.6$  their model is ruled out at a confidence level of  $2.5\sigma$ .

Note that the models need to predict only the average DLA cross section as a function of the halo mass, because the mean DLA bias does not depend on the scatter of the cross section for a fixed halo mass.

## 5.2 Constraints on the cross sections from the rate of incidence

The most recent determination of the rate of DLA incidence using the BOSS 9th Data Release shows that a fraction  $0.226 \pm 0.005$  of the sky is covered by a DLA with  $N_{HI} > 10^{20.3} \text{ cm}^{-2}$  in the redshift range  $2 < z < 3$ , as derived from the column density distribution in table 1 of [26] (the error quoted here is only the statistical one obtained from the same table, and does not include the systematic error due to corrections for incompleteness and impurity). This corresponds to a rate of incidence per unit of absorption pathlength,  $d\chi = (1+z)^2 H_0/H(z) dz$ , equal to  $0.066 \pm 0.002$ , which we assume to be constant with redshift. This observed rate of incidence fixes a required normalization of the relation of the DLA cross section and halo mass for any model.

We consider here a few examples and examine the value of the physical cross section  $\Sigma$  at the characteristic halo mass  $M_h = 10^{12} M_\odot$  to illustrate the typical implications of the observed rate of incidence and bias factor of DLAs:

1. A model with  $\alpha = 1$  and  $M_{min} = 10^9 M_\odot$ , which produces a bias  $b_D = 1.8$ , requires  $\Sigma(M = 10^{12} M_\odot) = 1400 \text{ kpc}^2$  to match the observed incidence rate. This is a factor of two larger than the cross section in the Q5 model of [47], and a factor 1.5 larger than the prediction of the momentum-driven wind model of [51].
2. A model with equation (5.2), with  $\alpha = 1$  and  $M_0 = 10^{10} M_\odot$ , matches our observed bias for  $\Sigma(M = 10^{12} M_\odot) = 2400 \text{ kpc}^2$ .
3. A model with equation (5.2), with  $\alpha = 0.5$ , needs an increased  $M_0 = 3 \times 10^{11} M_\odot$  to match the observed bias, and then requires  $\Sigma(M = 10^{12} M_\odot) = 4400 \text{ kpc}^2$ .

This illustrative example shows that the measured DLA bias factor can be matched either by an extended DLA host halo distribution with  $\alpha > 1$  and a low mass cutoff, or with a narrower range of halos around the characteristic mass of  $10^{12} M_\odot$ . A more extended distribution of halo mass reduces the required cross section because the rate of incidence is accounted for by a wider range of halo masses.

## 5.3 Consequences for the nature of DLAs

Generally, the models of DLAs discussed in the literature based on hydrodynamic simulations of structure formation fail to correctly predict the properties of DLAs for a common reason: the cross sections they predict for massive halos ( $M \simeq 10^{12} M_\odot$ ) are too small. The models that come closest to matching the observations are the Q5 model of strong winds in [47], which still predicts a rate of incidence and a baryonic content of DLAs that is a factor of 2 below the observed ones, and the momentum-driven wind model of [51], which with  $\alpha = 0.92$



would predict a DLA bias that is still  $2\sigma$  below our best value for  $\beta_F = 1$ , and cross sections that are too small by a factor  $\simeq 1.5$ .

Our observational result therefore implies that some neglected physical mechanism keeps the atomic gas spread out over an area larger than predicted by present models in host halos of massive galaxies. The natural expectation is that galactic winds that are even stronger than in the Q5 model of [47] and momentum-driven wind model of [51], and that have an increased impact on the halo gas distribution, are required. We emphasize, however, that DLAs in low-mass halos do not need to be further suppressed: in fact, these objects also help account for the total rate of incidence. The requirement for stronger winds is to allow atomic gas to stay at large radius over several orbits in massive halos.

To better understand the consequences of our result, we consider the Q5 model of [47] with all the cross sections increased by a factor two, to match both the bias factor and rate of incidence of DLAs. Then, the mean cross section in a  $10^{12} M_\odot$  halo with circular velocity  $v_c \simeq 200 \text{ km s}^{-1}$  at  $z = 2.3$  is  $\Sigma = 1400 \text{ kpc}^2$ . The corresponding proper radius containing the DLAs for a circular cross section is  $\sim 20 f_c^{-1/2} \text{ kpc}$ , or about 20% of the virial radius of the halo if the covering factor  $f_c$  is near unity, and the orbital period is  $\sim 5 \times 10^8 f_c^{-1/2} \text{ years}$ . These clouds can therefore complete no more than a few orbits at this radius over the age of the universe at  $z = 2.3$ , and would be forming a halo system that is dynamically supported by random motions, because the large radius implies that rotation may account for only a small fraction of the velocity dispersion.

The massive nature of most DLA host halos helps account for the large velocity widths observed for the metal lines associated with DLAs ([54], [55]), as noted also by [56]. At the same time, the problem of the rate of energy dissipation in DLAs ([57], [49]) is solved, because the long orbital periods imply long collision times among the DLA clouds, and the available gravitational energy that can be dissipated in cloud collisions is increased in massive halos.

Once the cross sections are known, we can infer the fraction of baryons present in DLA clouds if we make the simple assumption that the distribution of column densities is independent of halo mass, which is supported by the lack of dependence of our measured bias factor on column density. From table 1 in [26], we infer that the mean column density of all DLAs with  $N_{HI} > 2 \times 10^{20} \text{ cm}^{-2}$  is  $\bar{N}_{HI} = 7.8 \times 10^{20} \text{ cm}^{-2}$ . In a halo of  $10^{12} M_\odot$  of total mass and cross section  $\Sigma = 1400 \text{ kpc}^2$  (and using a hydrogen abundance by mass  $X = 0.76$ ), this implies that a fraction of 8% of all the baryons in the halo are in the form of atomic gas in the DLA clouds. Models with a narrower halo mass range as mentioned above, with higher required cross sections, would also require a larger baryon fraction in DLAs.

Finally, there may be a possible conflict with observations that limit the luminosity of galaxies associated with DLAs. In general, highly luminous galaxies have not been found in the proximity of DLAs, although there are cases where they are present: for example, a galaxy with a star formation rate of  $25 M_\odot/\text{yr}$  was found coincident with a DLA of very high column density by [58]. This star formation rate is just as expected for a  $10^{12} M_\odot$  halo dominated by a central galaxy, if as much as half of the baryons in the halo are turning to stars in a central galaxy over the age of the universe at  $z = 2.3$ . The lack of luminous galaxies in most other cases may have various explanations: the star formation rate in a massive halo may be distributed over several satellite galaxies, or maybe underestimated observationally because of dust absorption. Associated galaxies in massive halos may often be at rather large



impact parameters and may sometimes not be recognized for this reason. It is also likely that there is a large scatter in the relations of galaxy luminosity and DLA cross section to halo mass, and halos with luminous central galaxies may not be the same ones as halos with large DLA cross sections. We therefore do not think that our inferred large host halo mass for DLAs is necessarily in conflict with the rarity of luminous associated galaxies found so far. Precise observational upper limits on the mean luminosity of associated galaxies within at least 10 arc seconds of DLAs (corresponding to the expected halo virial radii) would be useful.

## 6 Conclusions

The first detection of the cross-correlation of DLAs with the Ly $\alpha$  forest absorption on nearby lines of sight is presented in this paper. The cross-correlation is well matched by linear theory predictions and shows strong evidence for the presence of redshift space distortions. We therefore believe that the excess Ly $\alpha$  absorption detected around DLAs is explained by the average large-scale gravitational mass inflow around the host halos of DLAs that is predicted when large-scale structure grows by gravitational evolution. We have used the amplitude of the cross-correlation to infer the bias factor of DLAs, related to the mass distribution of the host halos.

The new observational constraint of the bias factor of DLAs, together with the increasingly accurate determinations of the DLA rate of incidence, lead us to the conclusion that a majority of DLAs at  $z \sim 2$  to 3 arise in giant halos of atomic gas clouds around typical galaxies in dark matter halos of masses  $\sim 10^{12} M_{\odot}$ . A simple model that works well is that DLAs are present in all halos able to accrete photoionized gas ( $M > 10^9 M_{\odot}$ ), with a cross section  $\Sigma(M) \propto M^{\alpha}$ , with  $\alpha \simeq 1.1$  when  $\beta_F = 1$ , and slightly steeper for larger values of  $\beta_F$ . If the mean DLA column density is independent of halo mass, the value  $\alpha = 1$  corresponds to the case where a fixed fraction of the halo mass is present in the form of gas in the DLAs, so the observations do not require a large increase of the fraction of mass in DLAs with halo mass. However, the observations clearly imply that this gas in DLAs must be enormously extended in massive halos, with characteristic proper radii  $\sim 20 f_c^{-1/2} \text{ kpc} (M/10^{12} M_{\odot})^{\alpha/2}$  which are an increasing fraction of the virial radius as the halo mass increases.

This leads to a very different picture of high-redshift galaxies compared to their local counterparts: typical galaxies at  $z > 2$  are surrounded by atomic gas in the halo with column densities comparable to those in present galactic disks, but covering a much larger area and containing  $\sim 10\%$  of all the baryons in the halo, with kinematics that can only be dominated by random motions instead of rotation. This is clearly a fundamental fact that must be accounted for in any models of galaxy formation.

The cross-correlation with the Ly $\alpha$  forest can be used for other objects, such as quasars and metal-line systems, to study their relation with their large-scale environment and infer their bias factor. In the case of DLAs, we hope that their bias factor can be measured as a function of metallicity as soon as a rough measure of metal abundance can be obtained, which is difficult because of the low signal-to-noise of most of the BOSS spectra, the saturation of metal lines, and the ionization correction uncertainties. This would set constraints on the halo mass - metallicity relation and the correspondence to the mass-metallicity relation for galaxies.

## Acknowledgments

We would like to thank Joseph Hennawi, Patrick McDonald, Matt McQuinn, Uros Seljak, Anže Slosar and Matteo Viel for many illuminating discussions.

This research used resources of the National Energy Research Scientific Computing Center (NERSC), which is supported by the Office of Science of the U.S. Department of Energy under Contract No. DE-AC02-05CH11231, and was also supported by Spanish grants AYA2009-09745 and CSD2007-00060.

Funding for SDSS-III has been provided by the Alfred P. Sloan Foundation, the Participating Institutions, the National Science Foundation, and the U.S. Department of Energy Office of Science. The SDSS-III web site is <http://www.sdss3.org/>.

SDSS-III is managed by the Astrophysical Research Consortium for the Participating Institutions of the SDSS-III Collaboration including the University of Arizona, the Brazilian Participation Group, Brookhaven National Laboratory, University of Cambridge, Carnegie Mellon University, University of Florida, the French Participation Group, the German Participation Group, Harvard University, the Instituto de Astrofísica de Canarias, the Michigan State/Notre Dame/JINA Participation Group, Johns Hopkins University, Lawrence Berkeley National Laboratory, Max Planck Institute for Astrophysics, Max Planck Institute for Extraterrestrial Physics, New Mexico State University, New York University, Ohio State University, Pennsylvania State University, University of Portsmouth, Princeton University, the Spanish Participation Group, University of Tokyo, University of Utah, Vanderbilt University, University of Virginia, University of Washington, and Yale University.

## References

- [1] A. M. Wolfe, E. Gawiser, and J. X. Prochaska, *ARAA* **43**, 861 (Sep. 2005), [arXiv:astro-ph/0509481](#).
- [2] S. Cole, P. Norberg, C. M. Baugh, C. S. Frenk, J. Bland-Hawthorn, T. Bridges, R. Cannon, M. Colless, C. Collins, W. Couch, *et al.*, *Mon. Not. Roy. Astron. Soc.* **326**, 255 (Sep. 2001), [arXiv:astro-ph/0012429](#).
- [3] I. K. Baldry, K. Glazebrook, and S. P. Driver, *Mon. Not. Roy. Astron. Soc.* **388**, 945 (Aug. 2008), [0804.2892](#).
- [4] A. E. Shapley, *ARAA* **49**, 525 (Sep. 2011), [1107.5060](#).
- [5] J.-K. Krogager, J. P. U. Fynbo, P. Møller, C. Ledoux, P. Noterdaeme, L. Christensen, B. Milvang-Jensen, and M. Sparre, *Mon. Not. Roy. Astron. Soc.* **424**, L1 (Jul. 2012), [1204.2833](#).
- [6] R. K. Sheth and G. Tormen, *Mon. Not. Roy. Astron. Soc.* **308**, 119 (Sep. 1999).
- [7] J. L. Tinker, B. E. Robertson, A. V. Kravtsov, A. Klypin, M. S. Warren, G. Yepes, and S. Gottlöber, *Astrophys. J.* **724**, 878 (Dec. 2010), [1001.3162](#).
- [8] S. Cole and N. Kaiser, *Mon. Not. Roy. Astron. Soc.* **237**, 1127 (Apr. 1989).
- [9] J. Cooke, A. M. Wolfe, E. Gawiser, and J. X. Prochaska, *Astrophys. J.* **652**, 994 (Dec. 2006), [arXiv:astro-ph/0607149](#).

- [10] K. S. Dawson, D. J. Schlegel, C. P. Ahn, S. F. Anderson, E. Aubourg, S. Bailey, R. H. Barkhouser, J. E. Bautista, A. Beifiori, A. A. Berlind, *et al.*, ArXiv e-prints (Jul. 2012), 1208.0022.
- [11] D. J. Eisenstein, D. H. Weinberg, E. Agol, H. Aihara, C. Allende Prieto, S. F. Anderson, J. A. Arns, É. Aubourg, S. Bailey, E. Balbinot, *et al.*, *AJ* **142**, 72 (Sep. 2011), 1101.1529.
- [12] Vikas++, , submitted (2012).
- [13] A. Slosar, A. Font-Ribera, M. M. Pieri, J. Rich, J.-M. Le Goff, É. Aubourg, J. Brinkmann, N. Busca, B. Carithers, R. Charlassier, *et al.*, *JCAP* **9**, 1 (Sep. 2011), 1104.5244.
- [14] E. Komatsu, K. M. Smith, J. Dunkley, C. L. Bennett, B. Gold, G. Hinshaw, N. Jarosik, D. Larson, M. R. Nolta, L. Page, *et al.*, *Astrophys. J. Sup.* **192**, 18, 18 (Feb. 2011), 1001.4538.
- [15] SDSS-III Collaboration: Christopher P. Ahn, R. Alexandroff, C. Allende Prieto, S. F. Anderson, T. Anderton, B. H. Andrews, É. A. S. Bailey, R. Barnes, J. Bautista, T. C. Beers, *et al.*, ArXiv e-prints (Jul. 2012), 1207.7137.
- [16] A. S. Bolton, D. J. Schlegel, E. Aubourg, S. Bailey, V. Bhardwaj, J. R. Brownstein, S. Burles, Y.-M. Chen, J. E. Gunn, K. Dawson, *et al.*, ArXiv e-prints (Jul. 2012), 1207.7326.
- [17] J. E. Gunn, M. Carr, C. Rockosi, M. Sekiguchi, K. Berry, B. Elms, E. de Haas, Ž. Ivezić, G. Knapp, R. Lupton, *et al.*, *AJ* **116**, 3040 (Dec. 1998).
- [18] J. E. Gunn, W. A. Siegmund, E. J. Mannery, R. E. Owen, C. L. Hull, R. F. Leger, L. N. Carey, G. R. Knapp, D. G. York, W. N. Boroski, *et al.*, *AJ* **131**, 2332 (Apr. 2006), arXiv:astro-ph/0602326.
- [19] S. Smee, J. E. Gunn, A. Uomoto, N. Roe, D. Schlegel, C. M. Rockosi, M. A. Carr, F. Leger, K. S. Dawson, M. D. Olmstead, *et al.*, ArXiv e-prints (Aug. 2012), 1208.2233.
- [20] D. G. York, J. Adelman, J. E. Anderson, S. F. Anderson, J. Annis, N. A. Bahcall, J. A. Bakken, R. Barkhouser, S. Bastian, E. Berman, *et al.*, *AJ* **120**, 1579 (Sep. 2000).
- [21] I. Pâris, P. Petitjean, E. Aubourg, S. Bailey, N. P. Ross, A. D. Myers, M. A. Strauss, S. F. Anderson, E. Arnau, J. Bautista, *et al.*, ArXiv e-prints (Oct. 2012), 1210.5166.
- [22] N. P. Ross, A. D. Myers, E. S. Sheldon, C. Yèche, M. A. Strauss, J. Bovy, J. A. Kirkpatrick, G. T. Richards, É. Aubourg, M. R. Blanton, *et al.*, *Astrophys. J. Sup.* **199**, 3, 3 (Mar. 2012), 1105.0606.
- [23] C. Yèche, P. Petitjean, J. Rich, E. Aubourg, N. Busca, J.-C. Hamilton, J.-M. Le Goff, I. Paris, S. Peirani, C. Pichon, *et al.*, *A&A* **523**, A14, A14 (Nov. 2010).
- [24] J. A. Kirkpatrick, D. J. Schlegel, N. P. Ross, A. D. Myers, J. F. Hennawi, E. S. Sheldon, D. P. Schneider, and B. A. Weaver, *Astrophys. J.* **743**, 125, 125 (Dec. 2011), 1104.4995.
- [25] J. Bovy, J. F. Hennawi, D. W. Hogg, A. D. Myers, J. A. Kirkpatrick, D. J. Schlegel, N. P. Ross, E. S. Sheldon, I. D. McGreer, D. P. Schneider, *et al.*, *Astrophys. J.* **729**, 141, 141 (Mar. 2011), 1011.6392.
- [26] P. Noterdaeme, P. Petitjean, W. C. Carithers, I. Pâris, A. Font-Ribera, S. Bailey, E. Aubourg, D. Bizyaev, G. Ebelke, H. Finley, *et al.*, *A&A* **547**, L1, L1 (Nov. 2012), 1210.1213.
- [27] P. Noterdaeme, P. Petitjean, C. Ledoux, and R. Srianand, *A&A* **505**, 1087 (Oct. 2009), 0908.1574.
- [28] A. M. Wolfe, D. A. Turnshek, H. E. Smith, and R. D. Cohen, *Astrophys. J. Sup.* **61**, 249 (Jun. 1986).
- [29] R. J. Weymann, S. L. Morris, C. B. Foltz, and P. C. Hewett, *Astrophys. J.* **373**, 23 (May 1991).
- [30] Lee++, *The BOSS Lyman- $\alpha$  Forest Sample from SDSS Data Release 9*, , in preparation (2012).

- [31] K.-G. Lee, N. Suzuki, and D. N. Spergel, *AJ* **143**, 51, 51 (Feb. 2012).
- [32] N. Suzuki, D. Tytler, D. Kirkman, J. M. O’Meara, and D. Lubin, *Astrophys. J.* **618**, 592 (Jan. 2005).
- [33] I. Pâris, P. Petitjean, E. Rollinde, E. Aubourg, N. Busca, R. Charlassier, T. Delubac, J.-C. Hamilton, J.-M. Le Goff, N. Palanque-Delabrouille, *et al.*, *A&A* **530**, A50, A50 (Jun. 2011), 1104.2024.
- [34] K. N. Abazajian, J. K. Adelman-McCarthy, M. A. Agüeros, S. S. Allam, C. Allende Prieto, D. An, K. S. J. Anderson, S. F. Anderson, J. Annis, N. A. Bahcall, *et al.*, *Astrophys. J. Sup.* **182**, 543, 543 (Jun. 2009), 0812.0649.
- [35] C.-A. Faucher-Giguère, J. X. Prochaska, A. Lidz, L. Hernquist, and M. Zaldarriaga, *Astrophys. J.* **681**, 831 (Jul. 2008), 0709.2382.
- [36] P. McDonald, U. Seljak, S. Burles, D. J. Schlegel, D. H. Weinberg, R. Cen, D. Shih, J. Schaye, D. P. Schneider, N. A. Bahcall, *et al.*, *Astrophys. J. Sup.* **163**, 80 (Mar. 2006), arXiv:astro-ph/0405013.
- [37] J. K. Adelman-McCarthy, M. A. Agüeros, S. S. Allam, C. Allende Prieto, K. S. J. Anderson, S. F. Anderson, J. Annis, N. A. Bahcall, C. A. L. Bailer-Jones, I. K. Baldry, *et al.*, *Astrophys. J. Sup.* **175**, 297 (Apr. 2008), 0707.3413.
- [38] Busca++, , in preparation (2012).
- [39] A. Font-Ribera and J. Miralda-Escudé, *JCAP* **7**, 28 (Jul. 2012), 1205.2018.
- [40] P. McDonald, *Astrophys. J.* **585**, 34 (Mar. 2003), arXiv:astro-ph/0108064.
- [41] B. Efron and G. Gong, *American Statistician* **37**, 36 (1983).
- [42] N. Kaiser, *Mon. Not. Roy. Astron. Soc.* **227**, 1 (Jul. 1987).
- [43] A. J. S. Hamilton, *Astrophys. J. Let.* **385**, L5 (Jan. 1992).
- [44] N. Katz, D. H. Weinberg, L. Hernquist, and J. Miralda-Escudé, *Astrophys. J. Let.* **457**, L57 (Feb. 1996), arXiv:astro-ph/9509106.
- [45] J. P. Gardner, N. Katz, L. Hernquist, and D. H. Weinberg, *Astrophys. J.* **484**, 31 (Jul. 1997), arXiv:astro-ph/9609072.
- [46] J. P. Gardner, N. Katz, L. Hernquist, and D. H. Weinberg, *Astrophys. J.* **559**, 131 (Sep. 2001).
- [47] K. Nagamine, V. Springel, and L. Hernquist, *Mon. Not. Roy. Astron. Soc.* **348**, 421 (Feb. 2004).
- [48] K. Nagamine, A. M. Wolfe, L. Hernquist, and V. Springel, *Astrophys. J.* **660**, 945 (May 2007), arXiv:astro-ph/0510729.
- [49] A. O. Razoumov, M. L. Norman, J. X. Prochaska, J. Sommer-Larsen, A. M. Wolfe, and Y.-J. Yang, *Astrophys. J.* **683**, 149 (Aug. 2008), 0710.4137.
- [50] A. Pontzen, F. Governato, M. Pettini, C. M. Booth, G. Stinson, J. Wadsley, A. Brooks, T. Quinn, and M. Haehnelt, *Mon. Not. Roy. Astron. Soc.* **390**, 1349 (Nov. 2008), 0804.4474.
- [51] E. Tescari, M. Viel, L. Tornatore, and S. Borgani, *Mon. Not. Roy. Astron. Soc.* **397**, 411 (Jul. 2009), 0904.3545.
- [52] D. Erkal, N. Y. Gnedin, and A. V. Kravtsov, ArXiv e-prints (Jan. 2012), 1201.3653.
- [53] S. Bird, M. Vogelsberger, D. Sijacki, M. Zaldarriaga, V. Springel, and L. Hernquist, ArXiv e-prints (Sep. 2012), 1209.2118.
- [54] J. X. Prochaska and A. M. Wolfe, *Astrophys. J.* **487**, 73 (Sep. 1997), arXiv:astro-ph/9704169.
- [55] M. G. Haehnelt, M. Steinmetz, and M. Rauch, *Astrophys. J.* **495**, 647 (Mar. 1998),

arXiv:astro-ph/9706201.

- [56] L. A. Barnes and M. G. Haehnelt, *Mon. Not. Roy. Astron. Soc.* **397**, 511 (Jul. 2009), 0809.5056.
- [57] P. McDonald and J. Miralda-Escudé, *Astrophys. J.* **519**, 486 (Jul. 1999).
- [58] P. Noterdaeme, P. Laursen, P. Petitjean, S. D. Vergani, M. J. Maureira, C. Ledoux, J. P. U. Fynbo, S. López, and R. Srianand, *A&A* **540**, A63, A63 (Apr. 2012), 1202.0280.
- [59] M. Tegmark, *Phys. Rev. D* **55**, 5895 (May 1997).
- [60] U. . Seljak, *Astrophys. J.* **506**, 64 (Oct. 1998).

## A Effect of the Mean Transmission Correction on the cross-correlation

In section 3.3 the Mean Transmission Correction (MTC) has been introduced to reduce the variance in the total absorption of each individual spectrum. The MTC consists of renormalizing the transmitted fractions according to equations (3.5) and (3.7). This correction is nearly equivalent to requiring the mean perturbation  $\delta_{Fi}$  to be zero when averaged over each individual spectrum, except for the fact that the values of  $\bar{F}$  after the MTC are not exactly equal to  $\bar{F}_e$ , as shown in figure 3.

The correction was also applied for the study of the Ly $\alpha$  correlation function in [13] to reduce the variance arising from spectrophotometric errors. As noted there, the correction eliminates correlated absorption at all scales, systematically biasing the measured correlation function. A method to correct for this systematic bias when fitting a theoretical model to the observed correlation function was described in Appendix A of [13], which was tested with a set of mocks of Ly $\alpha$  spectra. Here, we derive an equivalent correction for the case of the cross-correlation of the Ly $\alpha$  forest with DLAs, or with any other objects with measured redshifts. For the MTC correction used in this paper, we consider only the simple case where all pixels have the same weight and instrumental noise is ignored, although the correction can be generalized to other cases. We also assume that the average of the corrected  $\delta_{Fi}$  in each spectrum is exactly zero.

Let  $\xi_{DF}(\sigma, \pi)$  be the true cross-correlation as a function of the comoving separation between the DLA and the Ly $\alpha$  pixel in the transverse and parallel directions in redshift space,  $\sigma$  and  $\pi$ . We consider a specific Ly $\alpha$  forest spectrum that extends from  $\pi_1$  to  $\pi_2$  in the parallel separation from the DLA. The corrected cross-correlation  $\xi_{DF}^{(q)}(\sigma, \pi)$ , measured after the average of  $\delta_F$  has been subtracted from the Ly $\alpha$  spectrum, is obtained by simply subtracting its value averaged over the range from  $\pi_1$  to  $\pi_2$ ,

$$\xi_{DF}^{(q)}(\sigma, \pi) = \xi_{DF}(\sigma, \pi) - \frac{1}{\pi_2 - \pi_1} \int_{\pi_1}^{\pi_2} d\pi' \xi_{DF}(\sigma, \pi'). \quad (\text{A.1})$$

The superindex ( $q$ ) on the corrected cross-correlation indicates that this function depends on the specific quasar spectrum and DLA, through the variables  $\pi_1$  and  $\pi_2$ .

A Ly $\alpha$  absorption spectrum measured in a quasar at redshift  $z_q$  starts and ends at absorption redshifts  $(1 + z_1) = \lambda_1(1 + z_q)/\lambda_\alpha$  and  $(1 + z_2) = \lambda_2(1 + z_q)/\lambda_\alpha$ , with  $\lambda_1 = 1041 \text{ \AA}$  and  $\lambda_2 = 1185 \text{ \AA}$  for the analysis presented in this paper. We neglect the fact that quasars

with  $z < 2.4$  have a Ly $\alpha$  spectrum starting at a higher redshift than  $z_1$  because of the wavelength range of the BOSS spectrograph. For a DLA at redshift  $z_D$ , the values of  $\pi_1$  and  $\pi_2$  for this particular spectrum are the comoving separation from  $z_D$  to  $z_1$  and  $z_2$ . The correction to apply (second term on the right hand side of equation A.1) to a given pair DLA-spectrum is then a function of  $z_D$  and  $z_q$ . Defining  $R$  as the comoving separation between  $z_D$  and  $z_q$ , we can express  $\pi_1$  and  $\pi_2$  as a function of  $R$  and  $z_D$ .

In practice we calculate the correction as a function of  $R$  only, by considering that all our systems are at redshift  $z_D = 2.3$ , which is the median redshift of the Ly $\alpha$  forest pixels weighted by their contribution to our cross-correlation measurement, and we neglect the changes with redshift except when we measure the cross-correlation at different redshift intervals in section 4.8. In order to compute the integral in the right hand side of equation A.1 we use the linear theory described in section 3.

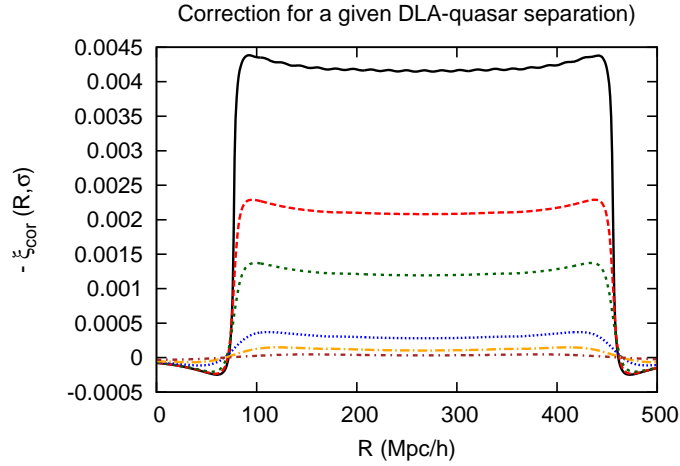


**Figure 15.** The correction  $\xi_{cor}(\sigma, R)$  as a function of DLA-quasar radial separation  $R$ , for different values of  $\sigma$  (from top to bottom): (1, 5, 10, 30, 50, 100) comoving  $h^{-1}$  Mpc.

The correction to the cross-correlation function is defined as

$$\xi_{cor}(\sigma, R) \equiv \xi_{DF}(\sigma, \pi) - \xi_{DF}^{(q)}(\sigma, \pi) = \frac{1}{\pi_2 - \pi_1} \int_{\pi_1}^{\pi_2} d\pi' \xi_{DF}(\sigma, \pi'). \quad (\text{A.2})$$

This correction depends on  $R$ , and on the fixed wavelengths  $\lambda_1$  and  $\lambda_2$ , but not on  $\pi$ . The function  $\xi_{cor}$  is shown in figure 15 as a function of  $R$  for several values of  $\sigma$ , evaluated at  $z_D = 2.3$

The correction is symmetric with respect to a sign change of  $R - R_c$ , where  $R_c \simeq 265 h^{-1}$  Mpc is the value of  $R$  when the DLA redshift is at the center of the forest, i.e.,  $\pi_1 = -\pi_2$ . The absolute value of the correction drops sharply for  $R > 455 h^{-1}$  Mpc or  $R < 75 h^{-1}$  Mpc (or equivalently,  $\pi_1 > 0$  or  $\pi_2 < 0$ , respectively), when the DLA redshift is outside the Ly $\alpha$  forest region of the quasar and the strongest contribution to  $\xi_{cor}$  near  $\pi = 0$  is outside the range of the integral in equation (A.2).

To obtain the average effect on the cross-correlation when measured over our entire sample of DLAs and quasar spectra, we define the function  $p(R|\pi)$  to be the conditional

probability of  $R$ , given that a Ly $\alpha$  forest pixel is present at a comoving parallel separation  $\pi$  from a DLA. This conditional probability depends in a complex way on the redshift distribution of DLAs and quasars in our sample, but can easily be computed. The final correction to the cross-correlation is

$$\Delta\xi(\sigma, \pi) = \int dR \, p(R|\pi) \, \xi_{cor}(\sigma, R) . \quad (\text{A.3})$$

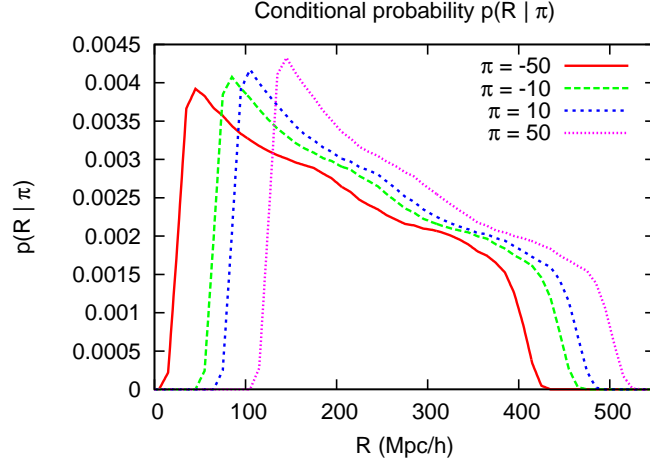


**Figure 16.** Conditional probability of  $R$  (DLA-quasar radial separation) given  $\pi$  (radial separation between the Ly $\alpha$  pixel and the DLA).  $p(R|\pi)$  is shown as a function of  $R$  for different values of  $\pi$ , computed for our sample of DLAs and quasar spectra.

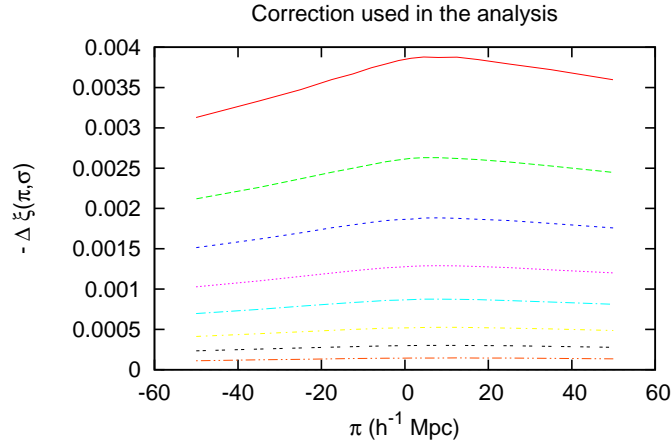


**Figure 17.** Final correction applied to the theoretical cross-correlation and used when fitting the DLA bias. The correction is shown as a function of radial separation  $\pi$  for different bins of  $\sigma$  (from top to bottom):  $1 < \sigma < 4 \, h^{-1} \text{ Mpc}$ ,  $4 < \sigma < 7 \, h^{-1} \text{ Mpc}$ ,  $7 < \sigma < 10 \, h^{-1} \text{ Mpc}$ ,  $10 < \sigma < 15 \, h^{-1} \text{ Mpc}$ ,  $15 < \sigma < 20 \, h^{-1} \text{ Mpc}$ ,  $20 < \sigma < 30 \, h^{-1} \text{ Mpc}$ ,  $30 < \sigma < 40 \, h^{-1} \text{ Mpc}$ , and  $40 < \sigma < 60 \, h^{-1} \text{ Mpc}$ .

In figure 16 we plot the conditional probability  $p(R|\pi)$  measured for the distribution of DLA and quasar redshifts in our sample, for four different values of  $\pi$ . This conditional



probability is approximately invariant if  $R - \pi$  is fixed, but not exactly so. The quantity  $p(R|\pi)$  is not symmetric under a change of sign of  $\pi$ , so the correction  $\Delta\xi(\sigma, \pi)$  is also asymmetric. This effect is seen in figure 17 which shows the correction we apply as a function of  $\pi$ , for the different bins of  $\sigma$  used in our analysis (increasing from top to bottom; see section 3.4).

In figure 9 (section 4) we plot the measured cross-correlation function, together with the best fit model, with and without the correction. The effect of this correction is clearly not crucial for our investigation, but will be more important for studies aiming to measure the cross-correlation on larger scales. We expect this to be more important when measuring the cross-correlation of quasars and the Ly $\alpha$  absorption, because of the larger number of quasars and their higher bias factor.

## B Optimal quadratic estimator

In section 3 our simple method to estimate the cross-correlation of Ly $\alpha$  absorption and the density of DLAs is described. In this appendix the precise optimal quadratic estimator for this cross-correlation is derived, assuming that the fields are Gaussian, and the assumptions required to obtain the simple estimator of equation (3.9) are described.

### B.1 Definitions and notation

The estimator of the fluctuation  $\delta_{Fi}$  at each pixel  $i$  in the whole set of quasar spectra is

$$d_i^F \equiv \frac{f_i}{\bar{f}_i} - 1 = \delta_{Fi} + \frac{N_i}{\bar{f}_i}, \quad (\text{B.1})$$

where  $f_i$  is the measured physical flux,  $\bar{f}_i = C_i \bar{F}_i$  is the averaged value of  $f_i$  at redshift  $z_i$ , and  $N_i$  is the noise, which is assumed to have a Gaussian distribution with variance  $\langle N_i^2 \rangle$ . The covariance matrix of this estimator is, neglecting any errors from the continuum fit,

$$C_{ij}^F \equiv \langle d_i^F d_j^F \rangle = \xi_F(\mathbf{r}_{ij}) + \frac{\langle N_i^2 \rangle}{\bar{f}_i^2} \delta_{ij}^K, \quad (\text{B.2})$$

where  $\xi_F(\mathbf{r}_{ij})$  is the correlation function of the Ly $\alpha$  fluctuation in the two pixels separated by  $\mathbf{r}_{ij}$  and  $\delta^K$  is the Kronecker delta function. This matrix is the same as  $C_{ij}$  in equation 3.12, except that the continuum fit errors are not included in the analysis of this appendix.

The other ingredient that we need to model is the overdensity of detected DLAs. Our discussion is completely general and applicable to any set of detected objects that are cross-correlated with the Ly $\alpha$  forest, and we refer to these detected objects in a specific survey as systems. We divide the survey volume in redshift space into  $N_c$  small cells of volume  $V_c$ , such that the number  $h_i$  of systems detected in each cell  $i$  is either 0 or 1, and the mean number of systems per cell,  $\bar{h}_i$ , is much smaller than one. The overdensity in a cell,  $\delta_{hi}$ , is defined according to

$$h_i = \bar{h}_i [1 + \delta_{hi}] + \epsilon_i, \quad (\text{B.3})$$



where  $\epsilon_i$  is the shot-noise, with 0 mean and a variance  $\sigma_{\epsilon_i}^2 = \bar{h}_i$ . The estimator of the density fluctuation from the measured systems in the survey is

$$d_i^H \equiv \frac{h_i}{\bar{h}_i} - 1 = \delta_{hi} + \frac{\epsilon_i}{\bar{h}_i} , \quad (\text{B.4})$$

and its associated covariance matrix  $C_{ij}^H$  is

$$C_{ij}^H \equiv \langle d_i^H d_j^H \rangle = \xi_H(\mathbf{r}_{ij}) + \frac{1}{\bar{h}_i} \delta_{ij}^K , \quad (\text{B.5})$$

where  $\xi_H(\mathbf{r}_{ij})$  is the correlation function of detected systems. In general, these detected systems may be associated with dark matter halos, and then  $\xi_H$  is the correlation function of halos weighted with their probability of yielding a detected system in the survey as a function of halo mass. This probability is the mean number of objects per halo when the detected systems are galaxies or quasars, or the cross section for the case of DLAs or metal absorption lines.

It is convenient to define a global data vector,

$$\mathbf{d} = (\mathbf{d}^F, \mathbf{d}^H) , \quad (\text{B.6})$$

of dimension  $N_F + N_c$ , where  $N_F$  is the total number of Ly $\alpha$  pixels and  $N_c$  the number of cells. The covariance matrix of the global data vector can be written as

$$\mathcal{C} = \begin{pmatrix} C^F & C^X \\ (C^X)^T & C^H \end{pmatrix} , \quad (\text{B.7})$$

where  $C^X$  is the covariance of the two fields,

$$C_{ij}^X = \langle d_i^F d_j^H \rangle = \xi_X(\mathbf{r}_{ij}) , \quad (\text{B.8})$$

and  $\xi_X(\mathbf{r}_{ij})$  is the quantity we want to obtain, the cross-correlation function of the Ly $\alpha$  absorption and the overdensity of systems. In this appendix the calligraphy letters  $\mathcal{C}$  are used for matrices with dimension  $(N_F + N_c) \times (N_F + N_c)$ . Generally, we are interested in measuring the cross-correlation in some bins in the separation (both the transverse and parallel components). Designating the bin number with a subindex  $\alpha$ , and the model value of the cross-correlation in this bin as  $\xi_\alpha$ , the matrix  $C^X$  can be expressed as:

$$C_{ij}^X = M_{ij}^\alpha \xi_\alpha , \quad (\text{B.9})$$

where  $M_{ij}^\alpha$  is a matrix with non-zero elements only when the separation between the pixel  $i$  and the cell  $j$ ,  $r_{ij}$ , lies inside the bin  $r_\alpha$ .

The derivative of the covariance matrix  $\mathcal{C}$  with respect to the cross-correlation  $\xi_\alpha$  in one of the bins is

$$\mathcal{C}_{,\alpha} = \begin{pmatrix} 0 & M^\alpha \\ M_\alpha^T & 0 \end{pmatrix} , \quad (\text{B.10})$$

and the covariance matrix is decomposed as

$$\mathcal{C} = \mathcal{C}_{,\alpha} \xi_\alpha + \mathcal{N} , \quad (\text{B.11})$$

with

$$\mathcal{N} = \begin{pmatrix} C^F & 0 \\ 0 & C^H \end{pmatrix} . \quad (\text{B.12})$$

## B.2 General solution

An unbiased quadratic estimator can generally be written as ([59],[60]):

$$\hat{\xi}_\alpha = (A^{-1})_{\alpha\beta} E_\beta , \quad (\text{B.13})$$

with

$$A_{\alpha\beta} = \text{Tr} [\mathcal{W} \mathcal{C}_{,\alpha} \mathcal{W} \mathcal{C}_{,\beta}] , \quad (\text{B.14})$$

and

$$E_\beta = \text{Tr} [\mathcal{W} \mathcal{C}_{,\beta} \mathcal{W} (\mathbf{d}\mathbf{d}^T - \mathcal{N})] , \quad (\text{B.15})$$

where  $\mathcal{W}$  is any symmetric matrix that we use to weigh our data vector.

For a Gaussian data vector, the optimal estimator is  $\mathcal{W} = \mathcal{C}^{-1}$ , and  $A$  is the Fisher matrix. Any other weight matrix  $\mathcal{W}$  still yields an unbiased estimator, but the estimator becomes more optimal as  $\mathcal{W}$  approaches  $\mathcal{C}^{-1}$ .

The expected value of the estimator is

$$\langle \hat{\xi}_\alpha \rangle = (A)_{\alpha\beta}^{-1} \langle E_\beta \rangle = (A)_{\alpha\beta}^{-1} \text{Tr} [\mathcal{W} \mathcal{C}_{,\alpha} \mathcal{W} (\mathcal{C} - \mathcal{N})] = (A)_{\alpha\beta}^{-1} A_{\beta\gamma} \xi_\gamma = \xi_\alpha . \quad (\text{B.16})$$

## B.3 Approximations

Inverting covariance matrices is a computationally demanding process. Since we have thousands of spectra with hundreds of pixels, the matrix  $C^F$  is in practice impossible to invert, not to mention the matrix  $\mathcal{C}$ . Here, we explain the different approximations that one can do in order to get an estimator that is sub-optimal but realistic.

### Noise-dominated regime

The first approximation is to consider that the contribution of the cross-correlation to the covariance is negligible, i.e., we can approximate  $\mathcal{C}^{-1} \sim \mathcal{N}^{-1}$ . The weight matrix is then

$$\mathcal{W} = \mathcal{N}^{-1} = \begin{pmatrix} (C^F)^{-1} & 0 \\ 0 & (C^H)^{-1} \end{pmatrix} . \quad (\text{B.17})$$

The product  $\mathcal{W} \mathcal{C}_{,\alpha}$  is:

$$\mathcal{W} \mathcal{C}_{,\alpha} = \begin{pmatrix} 0 & (C^F)^{-1} M_\alpha \\ (C^H)^{-1} M_\alpha^T & 0 \end{pmatrix} . \quad (\text{B.18})$$

We can now compute  $E_\alpha$  and  $A_{\alpha\beta}$  for this weighting:

$$E_\alpha = \text{Tr} [\mathcal{N}^{-1} \mathcal{C}_{,\alpha} \mathcal{N}^{-1} (\mathbf{d}\mathbf{d}^T - \mathcal{N})] = 2\text{Tr} [(C^F)^{-1} M_\alpha (C^H)^{-1} \mathbf{d}_H \mathbf{d}_F^T] , \quad (\text{B.19})$$

and

$$A_{\alpha\beta} = \text{Tr} [\mathcal{N}^{-1} \mathcal{C}_{,\alpha} \mathcal{N}^{-1} \mathcal{C}_{,\beta}] = 2\text{Tr} [(C^F)^{-1} M_\alpha (C^H)^{-1} M_\beta^T] . \quad (\text{B.20})$$

### Rare-objects regime

In this case the covariance matrix of the systems overdensity,  $C^H$ , will be dominated by the shot-noise, and we can do a second approximation for part of the weighting matrix:

$$C_{ij}^H \sim \bar{h}_i^{-1} \delta_{ij}^K. \quad (\text{B.21})$$

We can now simplify  $E_\alpha$  even further:

$$\begin{aligned} E_\alpha &= 2 \text{Tr} [(C^F)^{-1} M_\alpha (C^H)^{-1} \mathbf{d}_H \mathbf{d}_F^T] \\ &= 2 \sum_{i=0}^{N_F} \sum_{j=0}^{N_F} \sum_{k=0}^{N_c} \sum_{l=0}^{N_c} (C^F)_{ij}^{-1} M_{jk}^\alpha (C^H)_{kl}^{-1} d_l^H d_i^F \\ &= 2 \sum_{k=0}^{N_H} \sum_{i=0}^{N_F} \sum_{j=0}^{N_F} M_{jk}^\alpha F_{ij}^{-1} d_i^F, \end{aligned} \quad (\text{B.22})$$

where we have used that  $(C^H)_{ij}^{-1} d_j^H \sim \bar{h}_i d_i^H = (h_i - \bar{h}_i)$  equals to one when there is a system in the cell and zero otherwise, because the constant  $\bar{h}_i$  averages to zero when cross-correlated with the Ly $\alpha$  field  $d_F$ . The first summations in  $k$  and  $l$  are over the  $N_c$  cells in the volume, while the last summation in  $k$  is only over those  $N_H$  cells with a system on it.

The matrix  $A_{\alpha\beta}$  can also be simplified in a similar manner:

$$\begin{aligned} A_{\alpha\beta} &= 2 \text{Tr} [(C^F)^{-1} M_\alpha (C^H)^{-1} M_\beta^T] \\ &= 2 \sum_{i=0}^{N_F} \sum_{j=0}^{N_F} \sum_{k=0}^{N_c} \sum_{l=0}^{N_c} (C^F)_{ij}^{-1} M_{jk}^\alpha (C^H)_{kl}^{-1} M_{il}^\beta \\ &= 2 \sum_{k=0}^{N_H} \sum_{i=0}^{N_F} \sum_{j=0}^{N_F} M_{jk}^\alpha (C^F)_{ij}^{-1} M_{ik}^\beta. \end{aligned} \quad (\text{B.23})$$

The last expressions can be rewritten in a more compact form by defining a new matrix  $M'_\alpha$ , which has dimension  $N_H \times N_F$  (instead of  $N_c \times N_F$  for the matrix  $M_\alpha$ ) because it is defined only in the cells where a system is detected,

$$E_\alpha = 2 \text{Tr} [(C^F)^{-1} M'_\alpha \mathbb{1} \mathbf{1} \mathbf{d}_F^T], \quad (\text{B.24})$$

and

$$A_{\alpha\beta} = 2 \text{Tr} [(C^F)^{-1} M'_\alpha \mathbb{1} M'^T_\beta]. \quad (\text{B.25})$$

We have included the identity matrix  $\mathbb{1}$  and vector  $\mathbf{1}$ , both with dimension  $N_H$ , to ease the reference to the previous expressions.

### Independent-spectra regime

Pixels of two different spectra are only weakly correlated, especially in the limit of low quasar density where the typical separation between quasar lines of sight is large. In this limit, an additional approximation can be made for the weighting matrix in which only pixels from

the same spectrum are correlated. Then, the correlation matrix  $C^F$  and its inverse are block diagonal, with a block  $C_q^F$  for each quasar:

$$C^F = \begin{pmatrix} C_1^F & 0 & \dots & 0 & \dots & 0 \\ 0 & C_2^F & \dots & 0 & \dots & 0 \\ \dots & \dots & \dots & \dots & \dots & \dots \\ 0 & 0 & \dots & C_i^F & \dots & 0 \\ \dots & \dots & \dots & \dots & \dots & \dots \\ 0 & 0 & \dots & 0 & \dots & C_{N_q}^F \end{pmatrix}. \quad (\text{B.26})$$

Instead of having to invert a matrix of size  $N_F \times N_F$  (with  $N_F \sim 5 \times 10^7$ ) we need only  $N_q$  matrices of size  $N_p \times N_p$ , where  $N_q \sim 10^5$  is the number of spectra and  $N_p \sim 500$  is the number of pixels in a typical spectrum.

### Independent-pixels regime

Our final approximation is that each pixel in the spectrum is independent. In this case the matrix  $C^F$  is no longer block diagonal, but diagonal:

$$C_{ij}^F = \xi_{ij}^F + \frac{\langle N_i \rangle^2}{\bar{f}_i^2} \delta_{ij}^K \sim \sigma_{Ti}^2 \delta_{ij}^K, \quad (\text{B.27})$$

where  $\sigma_{Ti}^2 = \sigma_{Fi}^2 + \langle N_i \rangle^2 / \bar{f}_i^2$  is the total variance in the pixel, including the Ly $\alpha$  intrinsic variance.

The expressions for  $E_\alpha$  and  $A_{\alpha\beta}$  are now equal to

$$E_\alpha = 2 \sum_{k=0}^{N_H} \sum_{i=0}^{N_F} \sum_{j=0}^{N_F} M_{jk}^\alpha (C^F)_{ij}^{-1} d_i^F = 2 \sum_{k=0}^{N_H} \sum_{i=0}^{N_F} M_{ik}^\alpha w_i d_i^F, \quad (\text{B.28})$$

and

$$A_{\alpha\beta} = 2 \sum_{k=0}^{N_H} \sum_{i=0}^{N_F} \sum_{j=0}^{N_F} M_{jk}^\alpha (C^F)_{ij}^{-1} M_{ik}^\beta = 2 \sum_{k=0}^{N_H} \sum_{i=0}^{N_F} M_{ik}^\alpha w_i M_{ik}^\beta, \quad (\text{B.29})$$

where we have defined the pixel weight  $w_i = \sigma_{Ti}^{-2}$ .

We now see that the estimator in equation 3.9 corresponds to this case if we use only the diagonal part of  $A_{\alpha\beta}$ :

$$\hat{\xi}_\alpha = A_{\alpha\alpha}^{-1} E_\alpha = \frac{\sum_{k=0}^{N_H} \sum_{i=0}^{N_F} M_{ik}^\alpha w_i d_i^F}{\sum_{k=0}^{N_H} \sum_{i=0}^{N_F} M_{ik}^\alpha w_i M_{ik}^\alpha} = \frac{\sum_{k=0}^{N_H} \sum_{i \in \alpha} w_i d_i^F}{\sum_{k=0}^{N_H} \sum_{i \in \alpha} w_i}. \quad (\text{B.30})$$

If wide redshift bins are used with a substantial evolution of the signal being present within the bin, the estimator needs to be modified. In particular, equation B.9 should now be

$$X_{ij} = M_{ij}^\alpha \xi_\alpha \left( \frac{1 + z_{ij}}{1 + z_\alpha} \right)^\gamma, \quad (\text{B.31})$$

where we have assumed that the evolution of the cross-correlation is described by an amplitude varying as a power-law with the scale factor with an index  $\gamma$ . The simple estimator used in Section 3 needs to be modified as well, by multiplying the weights in equation 3.10 by the same factor.

We have not applied this correction for the weights, because the cross-correlation signal does not evolve strongly with redshift. In an Einstein-de Sitter universe, or at sufficiently high redshift to make the dark energy component negligible, the growth factor is proportional to the scale factor, and the value of  $\gamma$  is simply related to the evolution of the bias parameter:

$$\left(\frac{1+z_{ij}}{1+z_\alpha}\right)^\gamma = \left(\frac{b(z_{ij})}{b(z_\alpha)}\right)^2 \left(\frac{1+z_{ij}}{1+z_\alpha}\right)^{-2}. \quad (\text{B.32})$$

From the evolution of the line-of-sight Ly $\alpha$  forest power spectrum measured in [36], we can assume that the amplitude of the Ly $\alpha$  clustering evolves with  $\gamma_F = 3.8$ , implying that  $b_F$  evolves as  $(1+z)^{2.9}$ . Assuming that the DLA bias is constant over the redshift range, we obtain a value of  $\gamma_X = 0.9$  for the cross-correlation. This leads to a very small change over the narrow redshift range of our DLA sample.